Space Weather®

RESEARCH ARTICLE
10.1029/2022SW003165

Beyond Basic Drag in Interplanetary CME Modeling: Effects of Solar Wind Pileup and High-Speed Streams

C. Kay[1,2], T. Nieves-Chinchilla[1], S. J. Hofmeister[3], and E. Palmerio[4]

[1]Heliophysics Science Division, NASA Goddard Space Flight Center, Greenbelt, MD, USA, [2]Department of Physics, The Catholic University of America, Washington, DC, USA, [3]Leibniz Institute for Astrophysics, Potsdam, Germany, [4]Predictive Science Inc., San Diego, CA, USA

Key Points:

- We present a new model that simulates the development of a sheath as a coronal mass ejection (CME) propagates through the background solar wind
- Interactions between a CME and a high-speed stream can produce significant changes in the CME and CME-driven sheath
- These interactions have the largest effect when they occur close to the Sun or right before the CME reaches 1 au

Correspondence to:
C. Kay,
christina.d.kay@nasa.gov

Citation:
Kay, C., Nieves-Chinchilla, T., Hofmeister, S. J., & Palmerio, E. (2022). Beyond basic drag in interplanetary CME modeling: Effects of solar wind pileup and high-speed streams. *Space Weather*, *20*, e2022SW003165. https://doi.org/10.1029/2022SW003165

Received 23 MAY 2022
Accepted 3 AUG 2022

Abstract Coronal mass ejections (CMEs) cause severe space weather effects throughout our solar system. As a fast CME propagates through interplanetary space, it accumulates solar wind materials at its front. This pileup of materials, or CME-driven sheath, can be important in determining the geoeffectiveness of a CME. We take an existing arrival time model that includes expansion and deformation of the CME flux rope (ANTEATR; Kay & Gopalswamy, 2018, https://doi.org/10.1029/2018JA025780; Kay & Nieves-Chinchilla, 2021a, https://doi.org/10.1029/2020JA028911) and add a pileup procedure (PUP) as a physics-based approach to modeling the CME-driven sheath. ANTEATR-PUP solves the Rankine-Hugoniot equations for an oblique shock to determine the shock speed and sheath density, magnetic field, and temperature. The extra sheath mass affects the background drag calculation. Additionally, ANTEATR can now use any 1D profile for the background solar wind as opposed to the simple empirical models it previously relied upon. We present initial results from ANTEATR-PUP and compare with previous ANTEATR findings. Using results from an MHD simulation, we explore the effects of interactions with a static high-speed stream (HSS) on the CME's and sheath's interplanetary evolution. The drag forces essentially disappear while a CME remains within the HSS, but reappear stronger once the CME exits. The HSS-CME interaction produces the largest changes in the CME and sheath properties at 1 au when it occurs either close to the Sun near the inner simulation boundary at 0.1 au or right before the CME reaches 1 au. We estimate that these changes could significantly affect the geoeffectiveness.

Plain Language Summary The Sun has a constant outflow of material called the solar wind. This wind is a mix of "slow" and "fast" materials that forms structures as it flows out into the solar system. Periodically, the Sun explosively releases a more discrete bundle of materials and magnetic field known as a coronal mass ejection (CME). Often CMEs propagate faster than the solar wind but over time drag causes the CME's speed to decrease. As the CME moves through the solar wind, it accumulates materials at the front, analogous to snow on a snow plow. Accurately understanding these behaviors is essential for predicting how a CME could affect Earth. We combine a drag-based CME arrival time model with a new model for the formation of a sheath. We first consider a background of slow solar wind and then a background including a high-speed stream. The drag essentially disappears while the CME is within the high-speed stream. We determine how the interaction changes when it occurs at different distances, finding that the interaction could turn a moderate impact into a relatively intense impact at Earth if the high-speed stream is fairly large and the CME exits it right before reaching the Earth.

1. Introduction

Frequently, the Sun explosively releases a bundle of plasma and magnetic field known as a coronal mass ejection (CME). CMEs propagate out from the Sun through interplanetary space and can produce adverse effects when they interact with human technology at Earth or elsewhere in the solar system (e.g., Pulkkinen, 2007; Temmer, 2021). Understanding space weather effects associated with CMEs requires understanding the initial properties of a CME as it erupts from the Sun and how those properties evolve during its journey through interplanetary space as the CME interacts with the background solar wind.

The earliest forecasts of CME-driven space weather have focused on predicting the arrival time of CMEs. With advance knowledge of the timing of an impact, sensitive electronics can be powered down to better protect them, as was done for the Curiosity rover when a large CME impacted Mars in March of 2013, for example, These arrival

time models can be divided into several categories—empirical models (e.g., Gopalswamy et al., 2001; Paouris & Mavromichalaki, 2017), simple drag-based analytic models (e.g., Möstl et al., 2015; Vršnak et al., 2013), full fluid or magnetohydrodynamic (MHD) models (e.g., Jin et al., 2017; Odstrcil et al., 2004; Pomoell & Poedts, 2018; Shi et al., 2015), and machine learning models (e.g., Liu et al., 2018; Wang et al., 2019). Each style has advantages and disadvantages as there is a trade-off between model complexity (and potentially accuracy) and computation time, which can be important for scientific studies and real-time predictions.

Drag-based models tend to be useful as they are physics-driven but still run on time scales suitable for forecasting. In most of these models, a one-dimensional drag force is calculated from the CME speed and a simplified background solar wind speed. CMEs faster than the background decelerate, whereas slow CMEs accelerate, and these integrated effects determine the propagation time and CME speed upon impact. Typically, other properties, such as CME shape or size, are held constant.

The actual evolution of CMEs in interplanetary space is much more complicated than simply assuming that the drag gradually causes the CME speed to approach that of the background solar wind. Heliospheric imager observations show that while a CME's angular width maintains a nearly constant value during interplanetary propagation, its shape can change (e.g., Davies et al., 2021; Hinterreiter et al., 2021; Savani et al., 2010). The evolution in shape has been described as a "pancaking" behavior, where the radial extent shortens relative to the other directions (Riley & Crooker, 2004). CMEs are frequently described using a curved tube or torus-like shape. We refer to the axis running through the center of the tube as the toroidal axis and the cross section as a slice through the torus perpendicular to the toroidal axis. Pancaking can refer to a flattening of either the toroidal axis or the cross section. This change in shape can also be inferred from in situ measurements (e.g., Janvier et al., 2013; Owens & Cargill, 2004; Russell & Mulligan, 2002). While the majority of pancaking research focuses on the CME cross section, a similar "squashing" effect has been inferred for the central axis of CMEs (Janvier et al., 2013).

Any distortions in the CME shape and size will affect not only the arrival time but also its internal properties. It is essential to know the properties of a CME upon impact, particularly the magnetic field strength and orientation, as they affect the severity of any induced space weather effects. At Earth, a strong southward magnetic field (often referred to as B_z) causes the strongest space weather effects as it enhances magnetic reconnection between the solar wind structure and the Earth's magnetosphere (e.g., Gonzalez & Tsurutani, 1987; Yurchyshyn et al., 2005). While the evolution of internal properties is included in several analytic models (Durand-Manterola et al., 2017; Kumar & Rust, 1996; Mishra & Wang, 2018) and a natural result of more sophisticated MHD simulations (Török et al., 2018; Verbeke et al., 2019), currently most internal properties are not being routinely forecast.

Alternatively, instead of simulating the full interplanetary evolution, one can measure CME properties from remote observations and use those to orient a flux rope model and produce synthetic in situ observations (Kay et al., 2017; Kunkel & Chen, 2010; Savani et al., 2015). While this approach shows promise for predicting the magnetic field of a flux rope, it does not include any information about a CME-driven sheath, which can also produce significant space weather effects (e.g., Gonzalez et al., 1999; Tsurutani et al., 1988). When a CME propagates faster than the background solar wind, it accumulates solar wind plasma at its front, forming a dense sheath region. If the speed differential is large enough, a shock forms. Jian et al. (2006) found that over a full solar cycle, about two-thirds of CMEs had sheaths. Studies show that roughly a quarter or more of "intense" geomagnetic storms (as measured by Dst) are caused by shocks/sheaths (Lugaz et al., 2016 and references therein). Sheath regions tend to be highly turbulent, making accurate forecasts of their space weather effects difficult (Kilpua et al., 2017 and references therein), though Kilpua, Fontaine, et al. (2019) found some reoccurring patterns in a study of 89 sheaths. They found evidence for greater geoeffectiveness at the front and back of the sheath, where properties change rapidly between the preceding background solar wind and the sheath and the sheath and CME front, respectively.

Another factor typically unaccounted for in most simple interplanetary models is any encounter between a CME and another solar wind structure. By combining a mixture of remote and in situ observations, one can disentangle a complex interaction between a CME and a high-speed stream (HSS) or another CME (e.g., Heinemann et al., 2019; Kilpua, Good, et al., 2019; Nieves-Chinchilla et al., 2022; Winslow et al., 2021). Palmerio, Nieves-Chinchilla, et al. (2021) were able to track the interaction of two CMEs from the Sun out to 10 au. These interactions may be difficult to include in simple analytic models; nevertheless, they are important as the

strongest geomagnetic storms are caused by impacts that are a mix of structures rather than simply an isolated CME (Lugaz et al., 2016). For example, in September 2017, a series of CMEs erupted with the shock driven by a CME on 6 September catching up to and propagating into a CME that erupted on 4 September. Shen et al. (2018) estimated that the combined structure that arrived was twice as geoeffective (as measured by Dst) as if the CMEs arrived without any interaction. Similarly, Scolini et al. (2020) used an MHD model to explore the significance of CME–CME interaction on their geoeffectiveness and find that the interaction amplifies the magnitude of the magnetic field of the individual CMEs.

An interaction with background structures can also affect how CME structures are reconstructed within heliospheric imagers as shown recently by Barnard et al. (2022). They use synthetic images generated from a CME propagating in different backgrounds and reconstruct the CME trajectory using various geometric techniques. Comparison shows that the reconstructions tend yield larger distances than the "true" values as determined directly from the simulations themselves. Barnard et al. (2022) suggest that interactions with background structures tend to flatten the CME front relative to the flanks (pancake), which are often not accounted for in the geometric reconstruction. This causes the projected CME to appear at farther distances from certain viewpoints. This study shows the importance of understanding the evolution of a CME's shape as it propagates through a structured background.

To address some of the limitations described above, we present two major improvements to an analytic arrival time model that already includes the effects of CME expansion and deformation. First, we describe a method for developing a CME-driven sheath throughout its interplanetary propagation. Second, we explore the effect of a CME interacting with an HSS during its interplanetary propagation. Section 2 describes the analytic model, the incorporation of a sheath, and the solar wind backgrounds used in this study. Section 3 summarizes the general approach of this work and the inputs used for the model. In Section 4, before including any sheath development, we explore how the arrival time results change using a steady-state background that differs from the simplified background used in previous studies. In Section 5, we present results for the evolution of a sheath, first in a steady-state background and then with the inclusion of an HSS. Finally, in Section 6, we determine how the CME propagation and sheath evolution vary when the CME encounters the HSS at different heliocentric distances.

2. ANTEATR Pileup Procedure

We use ANother Type of Ensemble Arrival Time Results (ANTEATR; Kay & Gopalswamy, 2018) to simulate the interplanetary evolution of a CME. ANTEATR is a part of the Open Solar Physics Rapid Ensemble Information (OSPREI; Kay et al., 2022) suite that models the Sun-to-Earth evolution of CMEs. OSPREI includes a coronal CME deflection and rotation model (ForeCAT; Kay et al., 2015), which yields the change in a CME's latitude, longitude, and rotation, and an in situ model (FIDO; Kay et al., 2017), which creates synthetic profiles for the "observed" CME magnetic field vector and velocity, given a satellite location. ANTEATR was designed to bridge the gap between the other two models (ForeCAT → ANTEATR → FIDO), taking the position and orientation from ForeCAT, simulating the interplanetary evolution, and then passing the time of arrival and evolved CME properties to FIDO. ANTEATR can be run on its own, outside of the OSPREI suite, either for hypothetical cases or using coronal reconstructions for the initial properties of observed CMEs. In this work, we only introduce changes into ANTEATR and not the other components of OSPREI.

The earliest version of ANTEATR was a simple analytic model that performed a one-dimensional drag calculation for determining the CME speed but used a three-dimensional CME shape to determine a time of impact. ANTEATR treated the CME as a uniform, unmagnetized torus that maintained a constant shape and size. Kay and Nieves-Chinchilla (2021a) replaced ANTEATR's rigid torus with an actual flux rope using the elliptic-cylindrical model of Nieves-Chinchilla et al. (2018), yielding a Physics-driven Approach to Realistic Axis Deformation and Expansion within ANTEATR (ANTEATR-PARADE, hereafter PARADE for brevity). In addition to drag, PARADE includes the internal magnetic forces from a curved flux rope and thermal pressure. PARADE simulates the expansion and pancaking of the CME instead of simply assuming a static size and shape. Kay and Nieves-Chinchilla (2021a) presented the full details of the PARADE model and explores the significance of each individual force. The drag force tends to be the dominant force and will decelerate a fast CME or accelerate a slow CME. If the CME has higher pressure than the background solar wind, then the cross-sectional magnetic and thermal forces will cause the CME cross section to expand. Often a reasonable set of input parameters leads

to a slight overpressure that quickly equilibrates to the background pressure. If the drag deceleration is less than this brief expansion, it can lead to a brief acceleration of the CME front. We also include the axial magnetic force corresponding to the curved flux rope, but it tends to be negligible relative to the drag and cross-section expansion forces.

Kay and Nieves-Chinchilla (2021b) performed a parameter space exploration to better understand the correlation between PARADE inputs and outputs and found that the results depend on both CME properties and the properties of the background solar wind. To show that PARADE reproduces the behavior of real CMEs, rather than just being a theoretical experiment, OSPREI was updated to include the PARADE and was used by Kay et al. (2022) to mimic a forecasting approach for two recent Earth-impacting CMEs. The results are not restricted to only near-Earth trajectories: Palmerio, Kay et al. (2021) applied OSPREI to a CME that encountered Parker Solar Probe at 0.5 au in June 2020.

This is not the first time a component of OSPREI incorporated a model for a CME-driven sheath. Kay, Nieves-Chinchilla, and Jian (2020) added the ability for FIDO to include a Sheath Induced by the Transient (FIDO-SIT) in the synthetic in situ profile. The sheath profile is calculated solely based on the CME properties at the time of impact, rather than simulating its evolution over the full propagation. FIDO-SIT determines the shock and sheath properties using the Rankine-Hugoniot equations and the CME and solar wind properties. Kay, Nieves-Chinchilla, and Jian (2020) investigated several empirical and analytic methods for determining the sheath duration. The sheath properties then smoothly vary between the values at the shock and those at the ejecta; no turbulent fluctuations are included. FIDO-SIT was applied to four observed cases. Overall, good agreement was for the sheath properties, such as average magnetic field strength and density, but there was a clear room for improvement in the duration.

Here, we follow a similar approach to FIDO-SIT to determine the jump conditions at the shock or discontinuity separating the sheath and unperturbed solar wind. We replace the ad-hoc determination of the sheath properties at the time of impact with a simulation of their evolution during the CME's interplanetary propagation. This approach should improve our description of the sheath at the time of arrival as well us allowing us to better understand how it actually develops.

2.1. Rankine-Hugoniot Jump Conditions

The Rankine-Hugoniot jump conditions can be derived from the MHD equations, including Maxwell's equations. These jump conditions refer to the change in the properties of the regions immediately adjacent to either side of the shock. We note that this derivation is the fundamental basis of MHD shock physics and only outline the process here. We list the essential equations and how they apply to our CME-driven shock and for a full derivation, we direct the reader to Priest (1982).

We assume there is a time-independent solution that is invariant in the transverse or tangential direction, that is, the direction perpendicular to the shock normal. The jump conditions can be written as quantities conserved across the shock:

$$[\rho u_n] = 0 \tag{1}$$

$$\left[P + \rho u_n^2 + \frac{B_t^2}{2\mu_0}\right] = 0 \tag{2}$$

$$\left[\rho u_t u_n - \frac{B_t B_n}{\mu_0}\right] = 0 \tag{3}$$

$$\left[\frac{\rho u^2}{2} u_n + \frac{\gamma}{\gamma - 1} P u_n + \frac{B_t^2 u_n - B_t B_n u_t}{\mu_0}\right] = 0 \tag{4}$$

$$[B_n] = 0 \tag{5}$$

$$[u_n B_t - u_t B_n] = 0 \tag{6}$$

where the [ ] indicate the change in the property between the upstream and downstream regions. In these equations, ρ is the density, u is the speed, P is the pressure, B is the magnetic field, μ_0 is the permeability of free space, and the subscripts n and t refer to the normal and transverse directions, respectively.

Applying these jump conditions to a CME-driven shock, the upstream region is the unperturbed solar wind preceding the CME and the downstream region is the sheath. We assume that the solar wind properties are fully known and that the solar wind velocity and shock normal are both entirely radial in the local heliocentric coordinates. For now, we focus on results at the CME nose rather than near the flanks. We solve for an oblique shock so that solar wind magnetic field vector can point in any direction. Typically, the nonradial component of the solar wind magnetic field, $B_{\mathrm{SW},\perp}$, will fall in the longitudinal plane more so than the latitudinal one but we make no explicit assumptions of the actual direction in the derivation, only that the tangential plane fully includes $B_{\mathrm{SW},\perp}$.

The shock speed, v_{Shock}, and sheath density, magnetic field, and any transverse flow in the sheath, $v_{\mathrm{Sheath},\perp}$ are all unknown variables to be determined. We assume that the radial speed in the sheath is equal to the speed of the CME front in the stationary frame (v_{CME}), a reasonable assumption near the CME nose. We follow the common approach of switching to the de Hoffman-Teller (dHT) frame, where the magnetic field and velocity vector are parallel in both the upstream and downstream frames. This is accomplished by first boosting in the normal direction by v_{Shock} to a frame where the shock is stationary then boosting in the transverse direction by v_{dHT} so that the upstream $u_n B_t - u_t B_n$ is zero. Since this quantity is conserved, the value downstream will also be zero. We can determine the upstream and downstream velocities from the CME, solar wind, shock, and dHT velocities,

$$u_{un} = v_{\mathrm{SW}} - v_{\mathrm{Shock}} \tag{7}$$

$$u_{ut} = -v_{\mathrm{dHT}} \tag{8}$$

$$u_{dn} = v_{\mathrm{CME}} - v_{\mathrm{Shock}} \tag{9}$$

$$u_{dt} = v_{\mathrm{Sheath},\perp} - v_{\mathrm{dHT}} \tag{10}$$

but note that v_{Shock} and v_{dHT} are initially unknown so we must use other equations to close the system. We note that some may refer to the dHT velocity as the full boosted velocity combining the radial and transverse components. We only use v_{dHT} for the transverse component as the radial component has a tangible meaning as v_{Shock} in our applied situation.

The jump conditions can be combined in various forms to produce useful relations between the upstream and downstream properties. We can relate the density and the normal speeds using the compression ratio, r,

$$r = \frac{n_d}{n_u} = \frac{u_{un}}{u_{dn}} \tag{11}$$

where n represents the number density, which we find by dividing the density by the proton mass. We can combine the equations into a single expression, known as the shock adiabatic.

$$\left(\frac{\zeta M_A^2}{r} - \frac{c_s^2}{v_A^2}\right)\left(\frac{M_A^2}{r} - \cos^2\theta\right)^2 - \frac{M_A^2}{r}\sin^2\theta\left[\frac{M_A^2}{r}\left(\zeta + \frac{r-1}{2}\right) - \zeta\cos^2\theta\right] = 0 \tag{12}$$

where $\zeta = 0.5(\gamma + 1 - r(\gamma - 1))$, with γ being the adiabatic index, $c_s = \sqrt{\gamma P_u / n_u}$ is the upstream sound speed, $v_A = \sqrt{B_u^2/\mu_0 n_u}$ is the upstream Alfvén speed, $M_A = u_{un}/v_A$ is the upstream Alfvénic Mach number, and θ is the angle between the upstream magnetic field vector and the shock normal. Based on our assumptions near the CME nose, θ is equivalent to the angle between B_{SW} and the radial direction.

The shock adiabatic only still depends on two unknowns, r and M_A, but we can relate both of these to simply a dependence on v_{Shock} using Equations 7, 9 and 11. We numerically solve the shock adiabatic for the shock speed, which then gives us r, M_A, u_{un}, and u_{dn}. We can then find v_{dHT} from u_{un} and the upstream/solar wind magnetic field. The downstream density and the normal speed follow from Equation 11, the normal magnetic field is unchanged based on Equation 5, and the following relations, derived from the jump conditions, give the remaining parameters.

$$\frac{u_{dt}}{u_{ut}} = \frac{M_A^2 - \cos^2\theta}{M_A^2 - r\cos^2\theta} \tag{13}$$

$$\frac{B_{dt}}{B_{ut}} = r\frac{M_A^2 - \cos^2\theta}{M_A^2 - r\cos^2\theta} \tag{14}$$

$$\frac{P_d}{P_t} = 1 + \frac{\gamma u_{un}^2}{c_s^2}\left(1 - \frac{1}{r}\right) + \frac{1}{2}\sin^2\theta\frac{\gamma v_A^2}{c_s^2}\left(1 - \frac{r^2\left(M_A^2 - \cos^2\theta\right)^2}{\left(M_A^2 - r\cos^2\theta\right)^2}\right) \tag{15}$$

We assume an ideal gas so that the pressure is related to the temperature, T, by $P = nkT$, where k is the Boltzmann constant and we are only considering protons for simplicity. We note that our methodology applies to any scenario where v_{CME} is greater than v_{SW}, we can still solve for a compression region even if the velocity differential is too small to drive an actual shock. This process allows us to fully determine all of the downstream/sheath properties from the CME speed and upstream/solar wind properties at any point during a CME's interplanetary propagation.

2.2. Sheath Growth

Section 2.1 shows how we fully determine the conditions in the sheath region immediately adjacent to the shock. Here, we explain how we extend this to a simple model for the full sheath region.

We assume no sheath at the start of the simulation. A shock immediately forms moving at v_{Shock} as determined from the jump conditions. The shock moves away from the CME front at $v_{\mathrm{Shock}} - v_{\mathrm{CME}}$. Therefore, for a single time step Δt, the sheath width, w, grows as

$$\Delta w = (v_{\mathrm{Shock}} - v_{\mathrm{CME}})\,\Delta t \tag{16}$$

which can be converted to a time duration using v_{CME}. At the same time, the shock moves a distance $(v_{\mathrm{Shock}} - v_{\mathrm{SW}})$ Δt into the preceding solar wind. Whatever material was in this region is accumulated into the sheath so that the sheath mass grows as

$$\Delta M_{\mathrm{Sheath}} = n_{\mathrm{SW}} A_{\mathrm{Sheath}} (v_{\mathrm{Shock}} - v_{\mathrm{SW}})\,\Delta t \tag{17}$$

where A_{Sheath} is the cross-sectional area of the sheath, which we approximate as equal to the face-on area of our CME flux rope. The sheath density can be approximated as $n_{\mathrm{Sheath}} = M_{\mathrm{Sheath}}/A_{\mathrm{Sheath}}w$. While much of this follows from a common sense description of the process, it can also be derived from the continuity equation at the shock interface.

We assume constant density, velocity, temperature, and magnetic field strength within the sheath region, which is an oversimplification for a real, highly turbulent sheath but much of the variation is stochastic and cannot easily be incorporated into a simple deterministic model. We note that we use an instantaneous calculation of B and T, which should be accurate for the immediate region behind the shock at that time. Over time, we would expect these properties to settle toward a uniform sheath, but realistically this does not happen instantaneously. Future work will incorporate a more realistic, physics-driven model of the evolution within the sheath itself and allow for variation along the length of the sheath.

We also expect that there would be more systematic spatial variations in the transverse direction as one moves away from the nose toward the flank as the directions of the radial vector, shock normal vector, CME and solar wind velocities become misaligned and the jump conditions should be solved under slightly different assumptions. We acknowledge that this may introduce some errors into our determination of the sheath mass since we assume uniformity but leave the development of a higher-dimension sheath to a future work.

2.3. Effects on Drag Force

Since we now include the interplanetary development of a sheath structure, it is only appropriate to include its effects on the CME's interplanetary evolution. We include the mass of the sheath into the drag force calculation

as the CME and sheath are moving together and the extra inertia makes it more difficult to decelerate the CME-sheath structure. For a full description of the ANTEATR drag force, see Kay and Gopalswamy (2018).

The sheath structure will also affect the magnetic and thermal forces that affect the CME expansion and deformation. A critical aspect of these forces, particularly for the deformation, is determining the difference between the values at the nose and near the flanks. Since we only evaluate the jump conditions at the nose, we do not incorporate any changes into the expansion and deformation forces based on the presence of the sheath. These effects will be explored upon the development of the full nose-to-flank sheath model.

2.4. Solar Wind Background

All previous versions of ANTEATR have relied on simple analytic and empirical models for the background solar wind. We typically have assumed a constant solar wind velocity, a density profile that scales inversely with the square of the distance, and a Parker spiral magnetic field. The solar wind temperature scales with the distance to the power of −0.58, based off of Hellinger et al. (2013). For each ANTEATR simulation, we scale the solar wind background model to match given values at 1 au. These values are either provided as input or set to the average derived from OMNI values between 1963 and 2018 as was used in Kay, Mays, and Verbeke (2020). While this is an oversimplification of the actual solar wind, it reproduces the general solar wind behavior in the range that ANTEATR typically considers (the inner boundary usually set within 10–20 $R_{\odot}$, no restrictions on the outer boundary) but is simple enough that one can specify its free parameters in a real-time situation.

Instead of relying on these basic relations for the solar wind, we have now added the option for ANTEATR to use any one-dimensional profile of the background solar wind properties. ANTEATR reads in the number density, radial velocity, radial and longitudinal magnetic field strength, and temperature along a radial profile. At this time, we do not include any nonradial velocity or the latitudinal magnetic field as they tend to be significantly smaller than the other values and therefore have little effect on our results. Cubic splines are fit to the profile for each parameter, allowing us to interpolate values for any radial distance. This enables us to use a solar wind background provided by a more sophisticated fluid or MHD model. Forecasters currently run such models for real-time solar wind predictions, most of which could easily be adapted for ANTEATR use and facilitate ANTEATR's transition from research to operations.

In this study, we explore the effects of a CME interacting with an artificial HSS. The HSS properties are taken from a set of simulations performed with the European Heliospheric Forecasting Information Asset (EUHFORIA; Pomoell & Poedts, 2018), a 3D MHD model of the inner heliosphere starting at 0.1 au. We generated HSSs of different sizes and heliospheric latitudes within a slow solar wind environment by assuming a circular, idealized, coronal hole (CH) at the base of the solar corona. We assume that the CH expands at a fixed expansion factor of one up to 0.1 au to determine the cross-sectional area of the HSS at the inner boundary. We set homogeneous solar wind properties within the HSS at the inner boundary with a radial velocity of 650 km/s and a proton density of 150 cm^{-3}. Outside the HSS, the ambient solar wind was uniformly set to the velocity and density of 350 km/s and 500 cm^{-3}, respectively, at the inner boundary. The gas pressure was presumed to be 3.3 nPa and the magnetic field strength to be 217 nT, both in the HSS and in the ambient solar wind. Theses correspond to a coronal temperature of 1.6 MK and magnetic field strength of 1 G for the CH at the solar surface. In our MHD simulation, providing these values results in typical observed HSS velocities of 730 km/s and 5 cm^{-3} at 1 au for large CHs. We let these initial conditions relax for 17 days to yield a steady-state rotating HSS within a solar wind environment. During that relaxation time, the 3D HSS structure forms, including transition regions at the latitudinal flanks and a stream interaction region (SIR) between the HSS and the preceeding ambient solar wind. At 1 au, the size of the HSS and its velocity depend on the chosen size at the latitude of the CH. For more details on the simulation setup for the HSS, we refer to Hofmeister et al. (2020).

We extract profiles from the MHD results along a radial path within the solar equatorial plane between 0.1 and 1.2 au. The profiles contain both the ambient solar wind and the HSS with the HSS located at a farther distance for profiles extracted from later simulation times. We provided these profiles as an input to ANTEATR to study the effects of a structured background solar wind. In this work, we consider cases with the CH latitude centered at the equator and with CH areas between 10^9 km^2 and 2.5×10^{11} km^2, that is, small to large CHs. As such, the radial background profiles are all extracted from the latitudinal center of the HSS, which is also the direction of

the CME's propagation. We emphasize that within an ANTEATR simulation, the solar wind background does not evolve in time, but it serves as a static background profile.

Figure 1 shows the variation in HSS properties versus radial distance. R, for different simulation times (a) and CH areas (b). From top to bottom, the figure shows the number density n, the radial velocity v, the radial magnetic field B_r, the longitudinal magnetic field B_{lon}, and the temperature T. The black line shows the radial evolution of the ambient solar wind, that is, without an HSS, as a baseline. Figure 1a shows profiles for an 8×10^{10} km^2 CH at different times with darker colors corresponding to earlier times, with the HSS located closer to the Sun. Each HSS profile consists of a core region, related to the core of the CH, and transition regions where the properties settle to values of the ambient solar wind. The front transition region corresponds to the SIR and we refer to the core as the HSS plateau and the rear transition region as the HSS tail. The vertical dotted lines in Figure 1a delineate these three regions for the case shown in purple. Starting from the left, the tail is between the first and second lines, the plateau between the second and third lines, and the SIR between the third and fourth lines. Within the HSS plateau and tail, the velocity and temperature remain higher but the density and magnetic field fall below the ambient values. In the SIR, we see enhanced density, velocity, magnetic field strength, and temperature. This enhancement is due to a compression region forming between the HSS and slower preceding ambient solar wind, analogous to the development of a CME-driven sheath. The bottom panel shows the location of the SIR, plateau, and tail for each profile, which we define using the velocity. We find the maximum change in the velocity, $(\Delta v)_{\text{max}}$, from the ambient value, v_{amb}, and define the plateau as the region where $v > 0.95(\Delta v)_{\text{max}} + v_{\text{amb}}$. We define the edges of the SIR and tail where $v = 0.05(\Delta v)_{\text{max}} + v_{\text{amb}}$. When referring to the distance of the HSS front, we use the location where the longitudinal flow reverses the direction (not shown). Within the SIR, this longitudinal flow reversal refers to a deflection of the HSS plasma in the eastward direction, that is, along the Parker spiral, and a deflection of the preceding ambient solar wind in the westward direction, that is, in the direction of solar rotation. This definition allows for a precise identification of the HSS front. This location tends to

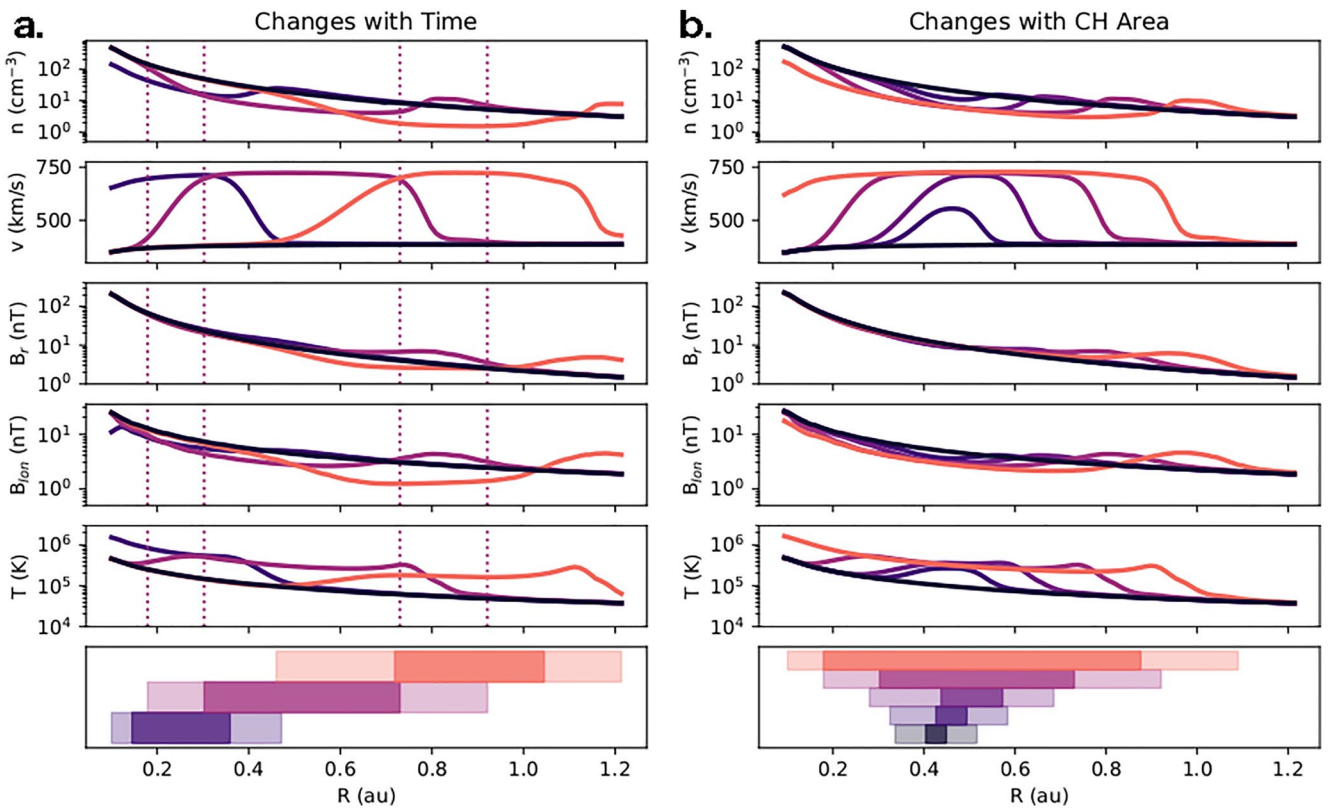

Figure 1. Solar wind properties versus heliocentric distance. Panel (a) shows profiles for a fixed CH area at different times (darker colors being earlier times), whereas panel (b) shows profiles for different CH areas at the same time (darker colors having smaller CH area). The dashed line shows the same profile in both panels and the black line represents a steady-state background. From top to bottom, the panels show the number density n, the radial velocity v, the radial magnetic field B_r, the longitudinal magnetic field B_{lon}, the temperature T, and a visual representation of the HSS location within each profile.

Table 1
ANTEATR Input Parameters

	CME			SW	
	Fast	Avg		K21	empMHD
v_F (km/s)	1,200	630	n (cm^{-3})	5.0	4.5
M_{CME} (10^{15} g)	10	5	v (km/s)	440	386
AW (°)	46	31	B (nT)	6.9	3.1
$AW_\perp$ (°)	18	10	log(T) (K)	4.79	4.66
δ_{Ax}	0.6	0.53			
δ_{CS}	0.6	0.7			
log(T_{CME}) (K)	5.88	5.59			
B (nT)	3,200	1,350			
B_0 (nT)	5,333	1,929			
T	1	1			
C	1.927	1.927			
Γ	1.33	1.33			
f_{Exp}	0.5	0.5			
C_d	1	1			
R_0 ($R_\odot$)	21.5	21.5			

be in roughly the center of the range we label the SIR. The profiles extracted from the MHD simulation ends at 1.2 au, so our profiles include cases where the HSS front has exited the outer boundary but the HSS plateau and tail are still present. We find that the front moves out approximately linearly for a given CH area and can use this relation to extrapolate the front position for later simulation times.

Figure 1a shows that, for a large HSS, the maximum HSS velocity remains roughly constant over time with a value just below 730 km/s. However, as time progresses, the SIR and tail become more extended, while the plateau comprises a smaller fraction of the HSS structure. In Figure 1b, we keep the MHD simulation time fixed but change the size of the CH, with darker colors representing smaller CH areas. In both panels of Figure 1, the violet line represents the same MHD background with the HSS front at 0.79 au and a CH area of 8×10^{10} km^2. For all but the smallest area (5×10^9 km^2), the plateau is centered around the same radial distance (about 0.5 au), but the width of the plateau increases significantly with CH area. The maximum HSS velocity increases with a CH area up to about 2×10^{10} km^2 and then saturates. The density, temperature, and magnetic field strength exhibit similar behavior to the velocity with the enhancement over the ambient values increasing over the smallest CH areas but saturating for larger areas.

3. Modeling Approach

Here, we briefly describe the inputs we must specify to run ANTEATR and the general setup of this project. Table 1 lists the inputs needed to describe the CME and an empirical background solar wind model (if not using an input background profile). For the CME, we must provide the initial radial velocity of the front, v_{CME}, the mass, M_{CME}, the full and perpendicular angular widths, AW and $AW_\perp$ (analogous to edge on and face on), the axial and cross-sectional aspect ratios, δ_{Ax} and δ_{CS}, the internal temperature, T_{CME}, the magnetic field strength, B, several flux rope properties, τ and C (for details, see Nieves-Chinchilla et al., 2018), the adiabatic index, γ, and the expansion factor f_{Exp}, which sets whether the CME is initially expanding self-similarly or convectively. We start the simulation at an initial distance, R_0, of 21.5 $R_\odot$ (0.1 au). The magnetic field strength, $B = \delta_{CS}\tau B_0$, is the toroidal field strength at the center of the CME. B_0 sets the overall magnetic field of the CME, which is converted into toroidal and poloidal magnetic field vectors at specific locations within the CME using the CME shape and the flux rope parameters. The poloidal field varies around the elliptical cross section. At the outer edge, it varies from $2\delta_{CS}B_0/\left(C\left(\delta_{CS}^2+1\right)\right)$ at the semiminor direction to $2\delta_{CS}^2 B_0/\left(C\left(\delta_{CS}^2+1\right)\right)$ at the semimajor axis. τ remains constant in our simulations but C evolves according to flux conservation. For further details on the inputs, we refer to Kay and Nieves-Chinchilla (2021a). The left portion of Table 1 shows our inputs for a fast and for an average CME, similar to what was used in Kay and Nieves-Chinchilla (2021a). We note that the "average" CME is actually slightly faster than average but we will refer to it as average for brevity.

The right portion of Table 1 shows the values we use for the empirical background solar wind. The "K21" values refer to the empirical background model scaled to match the 1 au OMNI averages as done in Kay and Nieves-Chinchilla (2021a). We also consider a version of the empirical model scaled so that the 1 au parameters match the values of the ambient MHD profile ("empMHD"). The K21 and empMHD models have the same dependence on distance for each parameter but the empirical coefficients are slightly adjusted to achieve different 1 au values. In contrast, we also use the baseline MHD profile corresponding to the ambient solar wind ("ambMHD"). This is the same MHD model as used in the HSS study, simply without adding an HSS. The ambMHD and empMHD profiles have the same 1 au values but need not vary with distance in the same manner. Use of these three backgrounds will help us disentangle the effects from changing how the background varies with distance (e.g., varying as R^{-2} or R^{-3}) versus simply shifting a profile toward higher or lower 1 au value (e.g., 400 or 450 km/s).

Table 2
Results for the Fast Coronal Mass Ejection (CME)

	No PUP			PUP					
Parameter	K21	empMHD	ambMHD	K21	empMHD	ambMHD	withHSS	Δ_-	Δ_+
v_F (km/s)	654	614	607	734	704	698	859	−9	379
v_{Exp} (km/s)	84	83	81	97	98	95	121	−2	65
AW (°)	50.0	50.9	51.1	49.4	50.2	50.4	48.2	−3.2	0.3
$\mathrm{AW}_\perp$ (°)	23.4	24.7	24.9	22.8	23.9	24.1	22.0	−2.8	0.3
δ_{Ax}	0.38	0.37	0.37	0.39	0.38	0.38	0.42	−0.004	0.067
δ_{CS}	0.38	0.38	0.37	0.40	0.39	0.39	0.44	−0.004	0.079
B_0 (nT)	70.1	65.0	66.4	68.9	63.9	65.0	63.0	−4.9	0.6
n_{CME} (cm^{-3})	7.8	7.0	6.9	8.2	7.4	7.3	8.8	−0.2	2.1
$\log(T_{\mathrm{CME}})$ (K)	4.82	4.81	4.81	4.83	4.82	4.82	4.84	−0.005	0.036
Transit time (hr)	45.1	46.4	47.0	42.4	43.2	43.7	36.4	−10.6	0.5
Duration (hr)	22.1	24.7	24.6	20.0	21.9	21.8	18.1	−6.9	0.3
R	—	—	—	3.57	3.86	3.85	3.92	−1.29	0.1
v_{Shock} (km/s)	—	—	—	897	867	858	1,111	−14	407
M_A	—	—	—	4.7	10.7	10.5	13.1	−6.6	8.2
Width ($R_\odot$)	—	—	—	33.2	32.0	32.3	26.5	−8.1	0.7
Duration (hr)	—	—	—	8.4	8.4	8.5	5.5	−6.9	0.3
M_{Sheath} (10^{15} g)	—	—	—	7.8	8.0	4.5	8.1	−6.6	0.4
n_{Sheath} (cm^{-3})	—	—	—	15.0	15.1	14.8	11.5	−9.5	0.6
$\log(T_{\mathrm{Sheath}})$ (K)	—	—	—	6.33	6.41	6.40	6.75	−0.74	0.49
B_{Sheath} (nT)	—	—	—	22.5	10.8	10.6	15.7	−7.8	8.6
θ_{Sheath} (°)	—	—	—	74.1	73.9	73.7	72.5	−16.9	0.3
$v_{\mathrm{Sheath},\perp}$ (km/s)	—	—	—	28.7	6.1	6.2	5.9	−4.1	8.9
Transit time (hr)	—	—	—	33.8	34.6	34.9	30.6	−6.9	0.4

Note. The left column lists the various output parameters with the top portion corresponding to CME parameters and the bottom to sheath parameters. The next three columns show results for ANTEATR-PARADE without the PUP component incorporated ("no PUP"). Each column is labeled by the name of the background solar wind model used for that run. This is followed by three columns for the same three background when PUP was included. The final three columns show the results for the run with an HSS background shown in Figure 2, followed by the maximum negative and positive changes in each parameter over all CH areas and HSS front distances.

We first run both the fast and average CMEs without including a sheath in the K21, empMHD, and the baseline, ambMHD backgrounds and discuss the difference in the results. We then perform the same simulations but including the new PUP features. Next, we introduce a single HSS background and compare how the forces differ between the ambMHD and this HSS case. We then expand to looking at the evolution of CME and sheath properties for each of the different background profiles shown in Figure 1a and at variations in the final properties for an ensemble of different CH areas and HSS front distances. Finally, we discuss how CME-HSS interactions at different distances affect different properties.

4. Changes in CME Propagation in Different SW Backgrounds

Tables 2 and 3 list ANTEATR results at 1 au for the fast CME and the average CME. The top half of each table shows the CME properties when the CME front reaches 1 au. The bottom half shows the sheath properties when the sheath front reaches 1 au. The "no PUP" section lists results for ANTEATR simulations with the PUP component deactivated, equivalent to the previous version ANTEATR-PARADE used in Kay and Nieves-Chinchilla (2021a). The "PUP" section lists ANTEATR-PUP results that make use of the new pileup procedure. The CME portion of the table includes the final values of v_{CME}, the expansion speed of the cross section, v_{Exp}, AW and $AW_\perp$, δ_{Ax} and

Table 3
Results for the Average Coronal Mass Ejection (CME) in the Same Format as Table 2

	No PUP			PUP					
Parameter	K21	empMHD	ambMHD	K21	empMHD	ambMHD	withHSS	Δ_-	Δ_+
v_F (km/s)	565	531	526	575	549	544	599	−4	117
v_{Exp} (km/s)	62	69	65	33	71	68	71	−3	18
AW (°)	33.4	35.1	35.1	33.3	34.9	34.9	33.8	−1.4	0.1
$\mathrm{AW}_\perp$ (°)	10.6	13.6	13.4	10.6	13.4	13.3	12.1	−1.2	0.1
δ_{Ax}	0.36	0.34	0.34	0.36	0.35	0.34	0.36	−0.002	0.028
δ_{CS}	0.70	0.64	0.62	0.70	0.64	0.63	0.66	−0.005	0.053
B_0 (nT)	17.4	13.2	14.0	17.4	13.1	14.0	14.4	−0.4	1.7
n_{CME} (cm^{-3})	17.3	11.7	12.0	17.4	11.9	12.2	15.3	−0.2	2.3
$\log(T_{\mathrm{CME}})$ (K)	4.57	4.52	4.52	4.57	4.52	4.52	4.55	−0.002	0.025
Transit time (hr)	62.3	63.8	64.4	61.8	62.8	63.4	60.0	−6.9	0.3
Duration (hr)	20.2	25.5	24.7	19.9	24.7	24.0	20.6	−4.5	0.04
R	—	—	—	2.42	3.49	3.46	3.39	−2.46	0.16
v_{Shock} (km/s)	—	—	—	680	629	623	699	−622	130
M_A	—	—	—	2.42	5.47	5.35	4.32	−5.35	2.61
Width ($R_\odot$)	—	—	—	42.2	25.7	26.0	13.9	−25.8	5.8
Duration (hr)	—	—	—	14.0	8.9	9.1	4.4	−9.1	1.7
M_{Sheath} (10^{15} g)	—	—	—	1.7	2.3	2.4	1.1	−2.4	0.1
n_{Sheath} (cm^{-3})	—	—	—	9.4	13.9	13.8	11.4	−12.2	10.9
$\log(T_{\mathrm{Sheath}})$ (K)	—	—	—	5.67	5.81	5.79	5.96	−0.829	0.259
B_{Sheath} (nT)	—	—	—	20.4	9.7	9.7	11.1	−8.3	7.9
θ_{Sheath} (°)	—	—	—	67.4	73.6	73.3	73.4	−45.4	1.5
$v_{\mathrm{Sheath},\perp}$ (km/s)	—	—	—	43.6	10.8	10.8	21.4	−10.7	13.2
Transit time (hr)	—	—	—	47.9	53.8	54.2	54.5	−3.5	2.8

δ_{CS}, B_0, the number density, n_{CME}, T_{CME}, and the transit time and duration. We present results in terms of B_0 rather than the toroidal or poloidal field, which depend on both B_0 and δ_{CS}.

We note that the K21 results here are not directly comparable to the analogous results in Kay and Nieves-Chinchilla (2021a). The previous study began ANTEATR simulations at 10 $R_\odot$, whereas here we start at 0.1 au (21.5 $R_\odot$) based on the bounds of the MHD simulations. We match the initial CME properties to the values in the previous simulation at 0.1 au to keep things as similar as possible, but we are missing any changes in expansion/deformation velocities resulting from forces acting upon the CME in the first 11.5 $R_\odot$ of propagation. The difference in the final results, while not entirely non-negligible, is small enough to have no systematic effect on the general results of this study.

Looking at both the fast and the average case, we find that the differences between the empMHD model and the ambMHD are small. This means that the empirical model does a reasonable job mimicking the radial variations in background solar wind parameters seen in the MHD model. It is not that there is absolutely no difference between the empMHD and ambMHD results. The backgrounds do slightly differ and the calculated forces can vary at individual distances, but the net effect of integrating these forces over the full simulation is minimal. As such, we suggest that there is no benefit to using an MHD profile instead of the empirical one for an ambient solar wind background. The empirical background is slightly more computationally efficient and will lead to essentially the same ANTEATR results, provided that one uses the appropriate 1 au scaling. We emphasize that this only applies to an unstructured, ambient background and we have only tested it with one MHD background. It remains possible that if the inner boundary were lower or the MHD model behaved significantly differently, the CME results may change.

We find larger differences between using the K21 and empMHD backgrounds. Again, these backgrounds have the same radial dependence for each solar wind parameter but K21 was scaled to match OMNI data at 1 au, whereas empMHD was scaled to match the ambient MHD profile. Between the two cases, the solar wind number density and temperature are reasonable similar, but the solar wind speed and magnetic field strength are much lower in empMHD than in K21. We see slightly more drag in the empMHD/ambMHD background than for the K21 background because of the decrease in solar wind velocity. This leads to a slower v_{CME}, a slightly longer transit time and duration, and small decreases in the CME magnetic field strength and density. While the difference between the ANTEATR results using the K21 and empMHD backgrounds is larger than that seen for comparing the empMHD and ambMHD backgrounds, the magnitude of any changes is still relatively small and does not fundamentally change the findings of any previous ANTEATR studies.

5. ANTEATR-PUP Results

Now, we explore the results of the new PUP component. The bottom sections of Tables 2 and 3 show the 1 au values of the sheath properties for the three different ambient backgrounds. This includes the compression, r, the shock speed, v_{Shock}, the Alfvénic Mach number, M_A, the sheath width and duration, the sheath mass and density, M_{Sheath} and n_{Sheath}, the temperature, T_{Sheath}, the magnetic field strength and orientation, B_{Sheath} and θ_{Sheath}, the transverse flow speed, $v_{Sheath,\perp}$, and the transit time of the shock.

5.1. Steady-State Background

First, we analyze how including the PUP component affects the propagation of CMEs within an ambient solar wind background, comparing the "no PUP" and "PUP" results in the top portion of Tables 2 and 3. For both the fast and average CMEs, the CME size, shape, and internal properties are largely unchanged. For the average CME, the transit time, duration, and velocities are largely unchanged, but for the fast CME, we see significant increases in the front speed (80–90 km/s). The changes in the expansion speed (increase of about 15 km/s) as well as transit time and duration (about 3 hr each) are less extreme but non-negligible. The drag force on the fast CME is more substantial than that on the average CME due to the larger speed differential, so increasing the inertia by adding the sheath mass produces larger changes in the final velocities for the fast case.

Figure 2 shows the evolution of sheath properties versus distance from the Sun. Here, we use the distance of the CME-driven shock rather than the distance of the front of the CME flux rope. We halt the ANTEATR-PUP simulations when the CME front reaches 1 au so the shock reaches some distance beyond this. Figure 2a shows results for the fast CME and (b) shows the average CME, both using the ambMHD background. Within each subfigure, each panel shows two parameters in black and maroon, which correspond, respectively, to v_{Shock} and v_{CME} (top left), r and M_A (top right), width and duration (middle left), M_{Sheath} and n_{Sheath} (middle right), B_{Sheath} and θ_{Sheath} (bottom left), and T_{Sheath} and $v_{Sheath\perp}$ (bottom right). In the velocity panel, we also include the background solar wind speed (dashed blue line) on the same scale as the other speeds.

Looking at the fast CME, we see that both v_{CME} and v_{Shock} decrease with distance, gradually approaching the background solar wind speed. v_{Shock} decreases slightly faster than v_{CME} with the difference between the two decreasing from about 300 km/s close to the Sun to 150 km/s at 1 au. The initial v_{CME} is about 800 km/s above v_{SW}. This leads to a strong shock with a compression near the maximum theoretical limit of 4, which can be derived from the shock adiabatic, assuming that M_A goes to infinity and $\gamma = 5/3$. Since it is near this fundamental limit, the compression only shows a small variation in magnitude over the full propagation. While v_{SW} remains nearly constant, the background Alfvén and sound speed decrease, which lead to a continual increase in the Mach number, even as v_{CME} decreases.

Both the sheath width and duration begin at zero and increase nearly linearly with distance, being 0.15 au wide and lasting 8.5 hr when reaching 1 au. Similarly, the sheath mass increases nearly linearly to 8.1×10^{15} g, which is about 80% of the total CME mass. The sheath density decreases over time. We assume the cross-sectional area of the sheath to increase over time, mirroring the CME driver's behavior, and we see the increase in the sheath width. These factors clearly outweigh the addition of new, piled-up mass over time, resulting in the reduction of sheath density with distance. The decrease in B_{Sheath} follows a very similar profile to n_{Sheath} and the orientation rotates from nearly radial to nearly perpendicular over time.

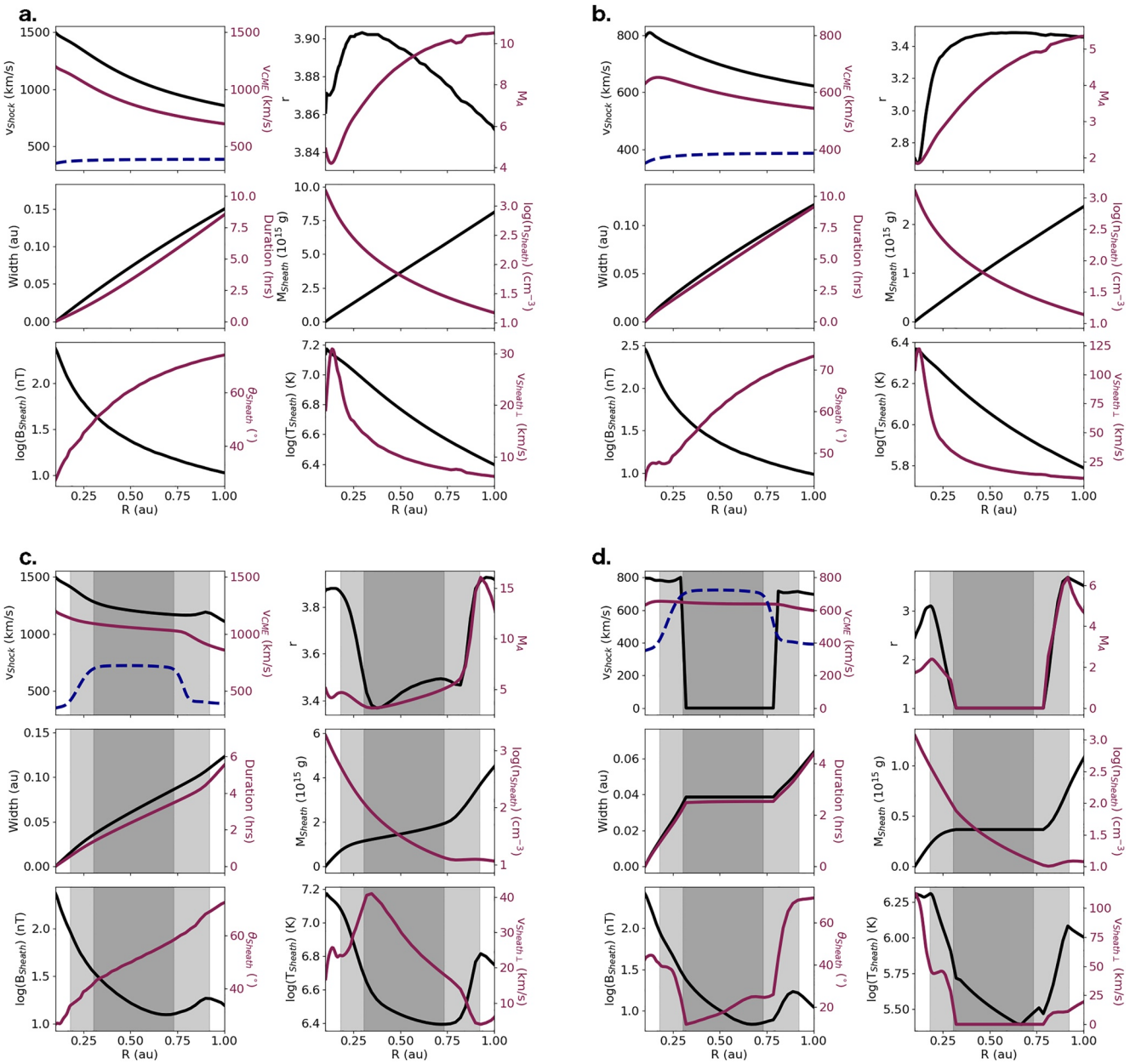

Figure 2. Evolution of sheath parameters. Panels (a and b) show results for an ambient background; panels (c and d) for a background with an high-speed stream. Panels (a and c) show results for the fast coronal mass ejection (CME), while (b and d) show the average CME. Within each subfigure, the panels show the shock speed, front speed and solar wind speed (top left; black, maroon, and dashed blue, respectively), the compression and Mach number (top right; black and maroon), sheath width and duration (middle left), sheath mass and density (middle right), the magnetic field strength and angle (bottom left), and the sheath temperature and transverse flow (bottom right).

The sheath temperature exceeds 10 MK close to the Sun, but this continually decreases to 2.5 MK near 1 au. The lateral flow speed within the sheath exhibits the inverse behavior of the Mach number with stronger flows during the times of low Mach number. From a purely hypothetical MHD perspective, when a shock is weaker, more materials are able to "escape" through lateral flow rather than becoming trapped between the driver and the shock. For a real CME, the actual lateral flow depends on the size and shape of the CME front and one's specific location in the sheath. When we only consider a single, simplified but representative value at the CME nose, we find that, given a constant Alfvén speed, the lateral flows scale inversely with the Mach number. The solar wind Alfvén speed decreases with distance so even while the Mach number increases with distance for the average CME, the lateral flow is less than 10 km/s when the sheath reaches 1 au.

For the average CME, the initial front speed is nearly half that of the fast CME so we see a much weaker shock, but much of the general behavior is similar. The CME speed shows a brief increase of 15 km/s close to the Sun, which results from the expansion of the CME cross section as the chosen properties are slightly overpressured relative to the background. The CME expansion creates pressure balance, the drag forces take over and the CME speed begins decreasing by 0.12 au. The shock speed mirrors the CME speed during this initial overexpansion.

The shock speed is initially 200 km/s faster than v_{CME} but this reduces to a difference of 80 km/s by 1 au. The Mach number increases from 2 to 5 as the background Alfvén and sound speeds decrease. The compression rapidly increases from 2.7 to 3.5, but then remains about constant. The remaining properties mirror the general behavior of the fast case, but with different magnitudes. The sheath width is slightly smaller but the speed is also slower, so that the total sheath duration is actually a bit longer at 9.1 hr. The sheath mass is 2.4×10^{15} g about half the CME mass. The 1 au sheath density and magnetic field strength are slightly smaller and the lateral flow speed slightly larger. The average CME has a much faster lateral flow than the fast CME close to Sun, which corresponds to its lower Mach number at this distance. At 1 au, the average case's temperature is noticeably lower at 0.6 MK.

5.2. Inclusion of High Speed Stream

Figures 2c and 2d are the same as Figures 2a and 2b, but for a background including an HSS. We use an HSS background originating from a CH with an area of 8×10^{10} km^2, that is, a medium to large CH, and extract a profile when the HSS front has reached 0.79 au, which is the violet line in both panels of Figure 1. For this background, the HSS tail begins around 0.18 au, the plateau exists between 0.30 and 0.73 au, and the SIR ends 0.92 au. The location of the HSS plateau of the HSS is shaded dark gray and the tail and SIR in light gray. The "withHSS" columns in Tables 2 and 3 show the 1 au results for this background.

Focusing first on the final CME properties for the fast CME, shown in Table 2, we find that there are significant increases of 161 km/s in the final v_{CME} and 25 km/s in v_{Exp} and decreases of 7.3 and 3.7 hr in the transit time and duration, respectively. The size, shape, and internal properties exhibit smaller but noticeable changes.

Looking at the evolution of the sheath for the fast case in Figure 2c, we see that the CME and sheath speed initially begin decreasing until the CME enters the HSS, while in the HSS plateau, the velocities exhibit a slow deceleration but remain nearly constant. Once the CME front reaches the SIR, the CME velocity begins decreasing but the shock velocity remains high until the CME reaches the ambient solar wind. The compression shows that the CME initially drives a strong shock, which weakens while within the HSS, but reappears stronger upon exit. The accumulation of materials into the sheath slows down while the CME is in the HSS, as evidenced by the flattening of the width, duration, and mass profiles. This is driven by the decrease in the background solar wind density within the HSS. We see local peaks in the temperature and magnetic field strength at the outer boundary of the SIR, right before the CME reaches the ambient solar wind. While within the SIR, the CME sheath is accumulating solar wind plasma that has already been piled up once due to its interaction with the HSS. This repeating piling-up of materials that peaks just as a CME exits an SIR could produce abnormally extreme geomagnetic effects at Earth. While such a scenario is not extremely common in the solar wind—Berdichevsky et al. (2005) estimated that only ∼8% of the 214 near-Earth CMEs reported in the Cane and Richardson (2003) catalog were propagating within a HSS—the outcomes of a CME–SIR interaction event can be particularly challenging for space weather forecasting. For example, the 18 September 2000 geomagnetic storm (see, e.g., Xue et al., 2005) reached a minimum Dst of −201 nT (i.e., corresponding to a major/extreme event) coinciding with a region of strongly negative B_z, high solar wind speed, and significantly enhanced plasma density due to an interaction between a CME-driven sheath and a preceding SIR.

For the average CME, shown in Figure 2d, we see similar effects but slightly smaller changes in the CME properties. The sheath begins forming as the CME propagates through the ambient solar wind and the tail of the HSS, but near the plateau, it reaches a point where the background speed exceeds that of the CME and a shock no longer forms. In effect, the HSS plasma in front of the CME runs away from the CME so no mass can be accumulated. For a more realistic background that evolves with time, the CME would never actually reach the HSS, which propagates faster and starts at a farther distance. If this CME erupted in front of the HSS, that is, erupting earlier from a more eastward longitude than the CH, the HSS plasma would pile up at the back of the CME and accelerate the CME. For now, our algorithm assumes that CME can propagate through the HSS, during which the

accumulation of materials in the CME-driven sheath simply ceases as we do not include any physics to allow for the sheath to begin dispersing. As such, the sheath mass and width remain constant. The CME and therefore our sheath still expand in the lateral directions, causing the sheath density to decrease.

When the background velocity exceeds that of the CME, the ANTEATR-PUP temperature and magnetic field strength reflect the background solar wind values since we instantaneously calculate them from the compression, which is now one. In this region, the ANTEAR-PUP temperature and magnetic field are not reliable as the full sheath adjust quasi-instantaneously to the background values rather than slowly approaching them over time. A more sophisticated approach is beyond the current scope of ANTEATR-PUP and we reiterate that with a time-dependent background, a CME could never propagate into and through a background region that moves faster than the CME itself.

5.3. Forces

To get a better sense of what is fundamentally happening during the encounter with the HSS, we next look at the different forces acting upon the CME within ANTEATR-PUP. These are the forces from ANTEATR-PARADE, described in Sections 2.3–2.5 of Kay and Nieves-Chinchilla (2021a). Figure 3 shows the acceleration from drag (maroon), axial magnetic forces (pink), cross-sectional magnetic forces (dark blue), and cross-sectional thermal forces (light blue). Figure 3a shows results for the fast CME and (b) shows the average CME. We show results for the three different HSS background profiles shown in Figure 1a, all using the 8×10^{10} km^2 area CH but at different times corresponding to HSS fronts at 0.42, 0.79, and 1.16 au (corresponding to 30 hr spacing in the MHD simulation). The region corresponding to the HSS is shaded in each panel in the same format as Figures 2c and 2d.

The solid lines show the accelerations when we use a background with an HSS and the dashed lines show the accelerations in the ambient background for comparison. The only noticeable change is in the drag force, none of the other ambient case accelerations can be distinguished from the results that include an HSS. The HSS properties vary from the ambient solar wind in density, velocity, magnetic field, and temperature. Both the cross-sectional magnetic and thermal forces depend on the pressure gradient relative to the solar wind background; yet the effects on the cross-sectional forces is minimal and not visible on the scale of these figures. The axial magnetic force does not explicitly include any solar wind background properties, so it is only altered by secondary effects, such as changes in the background causing changes in the CME shape, and it is less surprising that we see no obvious change in the axial magnetic forces.

For both the fast and average CMEs, we see that drag force essentially disappears while in the HSS tail and plateau. In these regions, the velocity differential between the CME and solar wind is smaller, and the background solar wind density is smaller, both of which decrease the drag. During this time, the CME retains a higher speed than it does in a steady-state background. Once the CME reaches the SIR, the background speed decreases, which increases the velocity differential. Simultaneously, the background density increases due to the solar wind pileup within the SIR. Both factors combine to increase the drag to values much larger than in the ambient solar wind. The closer to the Sun that the CME–HSS interaction occurs, the stronger the peak in the drag deceleration. Once the CME begins moving out of the SIR, the drag force gradually approaches the ambient case values.

6. Variations With HSS Properties

One of the major reasons for developing a strategically simplified model, such as ANTEATR-PUP, is that it allows us to perform ensembles with a large number of members. Previous ANTEATR studies have analyzed the changes in the outputs as we vary different input CME parameters. In the following ensemble runs, we use different solar wind background profiles to investigate the sensitivity of CME and sheath properties to interactions with HSS of different sizes and at different heliocentric distances. We perform simulations for 20 CH areas between 10^9 km^2 and 2.5×10^{11} km^2. The radial profiles of the HSS have been sampled at 6 hr resolution. The HSS corresponding to the smallest CH areas propagates out slower radially that the larger CH-area HSS. Accordingly, different size HSS are not at the same distance at the same time. We refer to our backgrounds by the position of the HSS front, rather than the simulation time. From our set of backgrounds, we remove all cases where the entire HSS is outside of 0.1–1.2 au. We perform an ensemble study for both the fast and average CMEs.

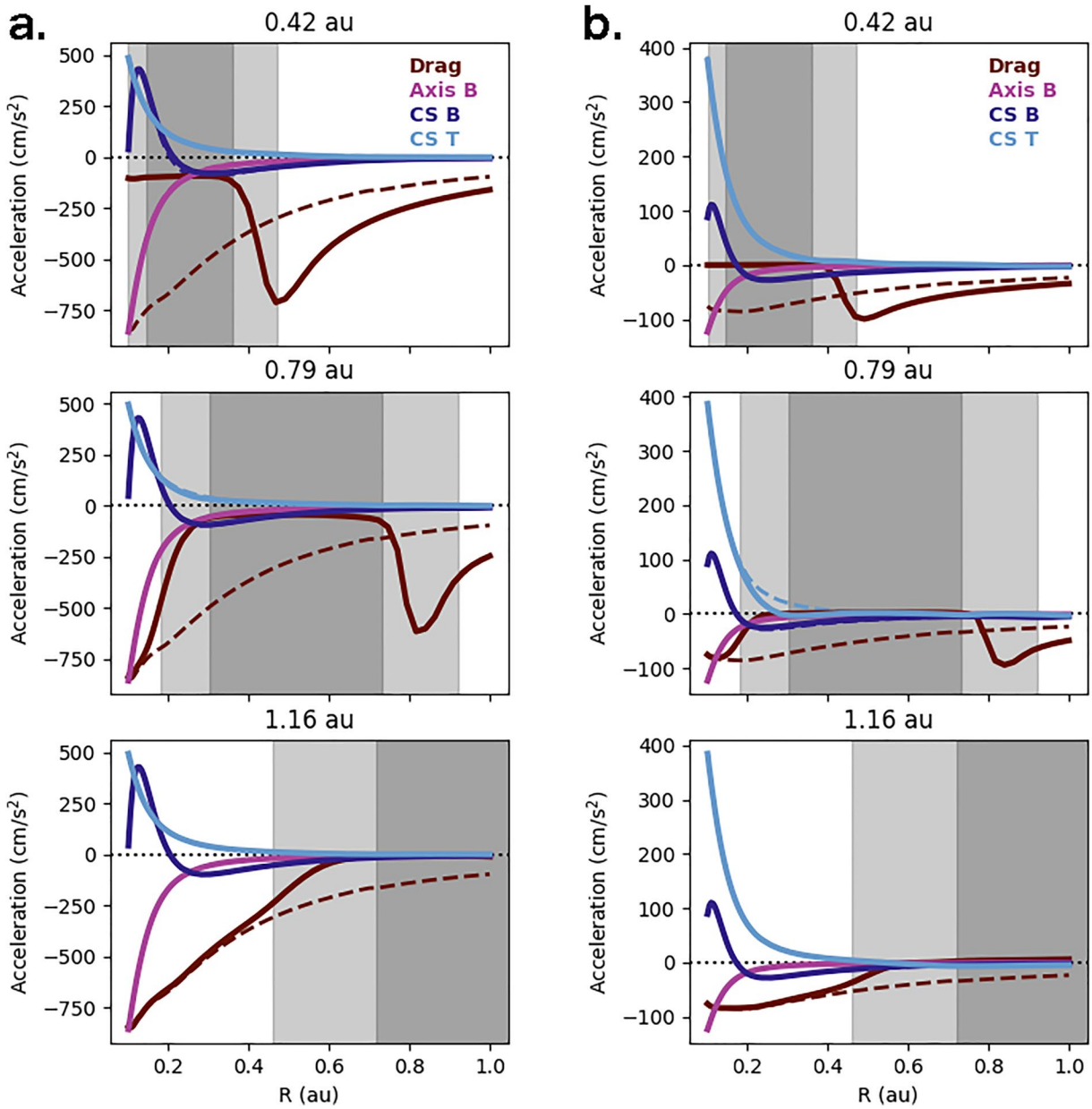

Figure 3. Forces acting upon the coronal mass ejection (CME). Panel (a) shows the fast CME and (b) the average CME. Within each subfigure, the six panels show results for three different background profiles with the high-speed stream (HSS) at different distances. The gray-shaded region shows the HSS tail, plateau, and stream interaction region, and the titles contain distance of the HSS front. The lines show the drag force (maroon), the axial magnetic force (pink), the cross-sectional magnetic force (dark blue), and the cross-sectional thermal force (light blue). The dashed lines indicate the forces for the case with an ambient background.

Figures 4–9 show results for different CMEs and sheath properties. Each row shows a different property. We do not include figures for every single parameter listed in Tables 2 and 3 as many parameters mirror the behavior of other parameters, but will comment on any significant trends when appropriate. In the left columns, we show the evolution of a property within each of the three HSS backgrounds shown in Figure 1a. The profiles are the colored the same as the background profiles in Figure 1a and we visually represent the HSS structure (tail, plateau, and SIR) and location within each background profile at the bottom of the panel. The black line represents the results from the ambient background.

For each run, we determine the difference between the value of a parameter at 1 au and the corresponding value in the ambient background. The right column shows this change for all CH areas and HSS front distances with red

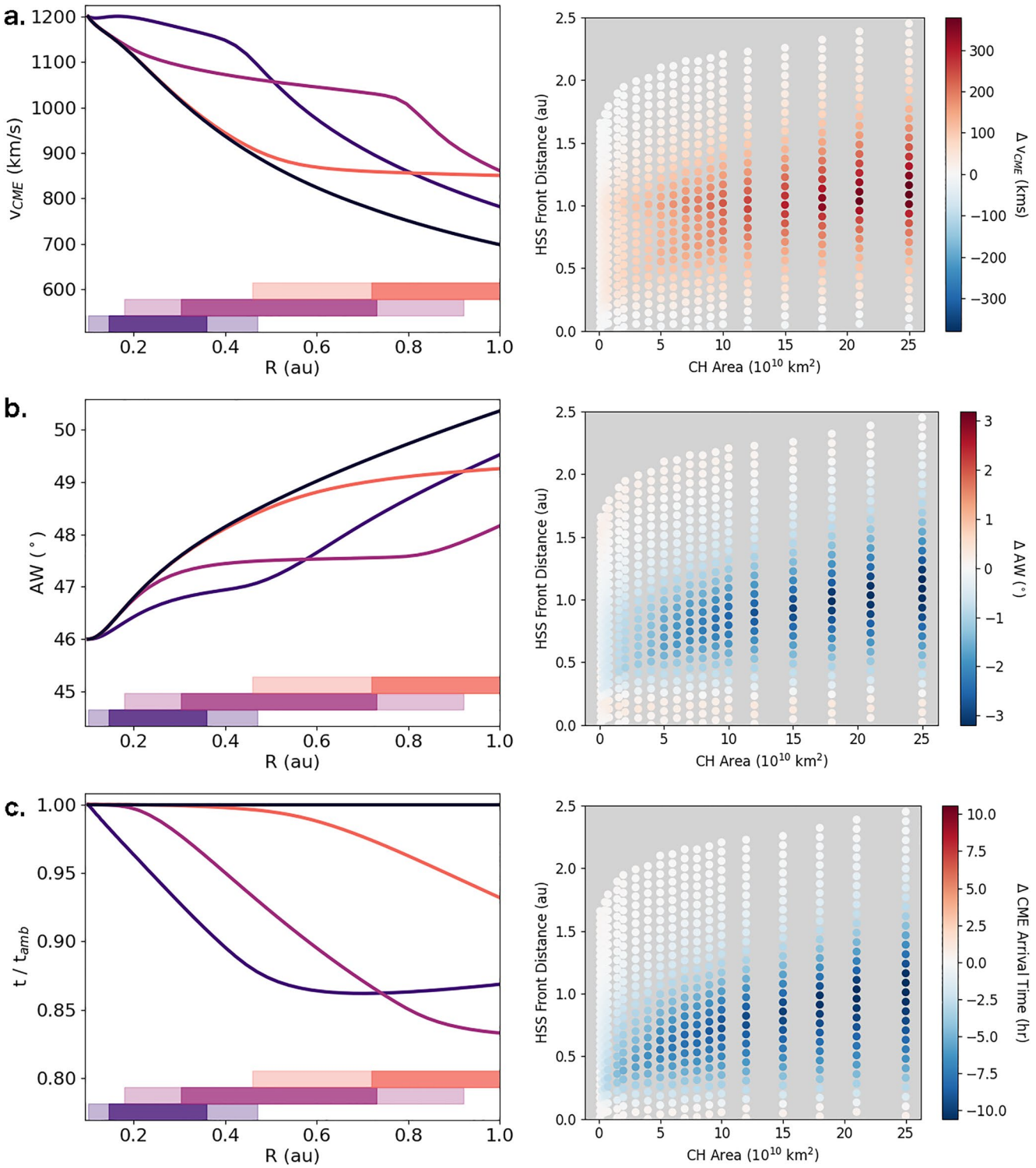

Figure 4. Pileup procedure results for the front velocity (top row), the angular width (middle row), and the transit time (bottom row) for the fast coronal mass ejection. The left column shows the evolution of a property versus distance. The black line shows results for the ambient background. The colored lines correspond to backgrounds with the high-speed stream (HSS) at different distances. The HSS locations are indicated by the colored bars at the bottom of each panel. The transit time is the time to reach that distance, and it is shown normalized to the ambient transit time to better visualize the changes. The right column shows the change in the final value of a parameter for all the different combinations of CH areas and HSS front distances.

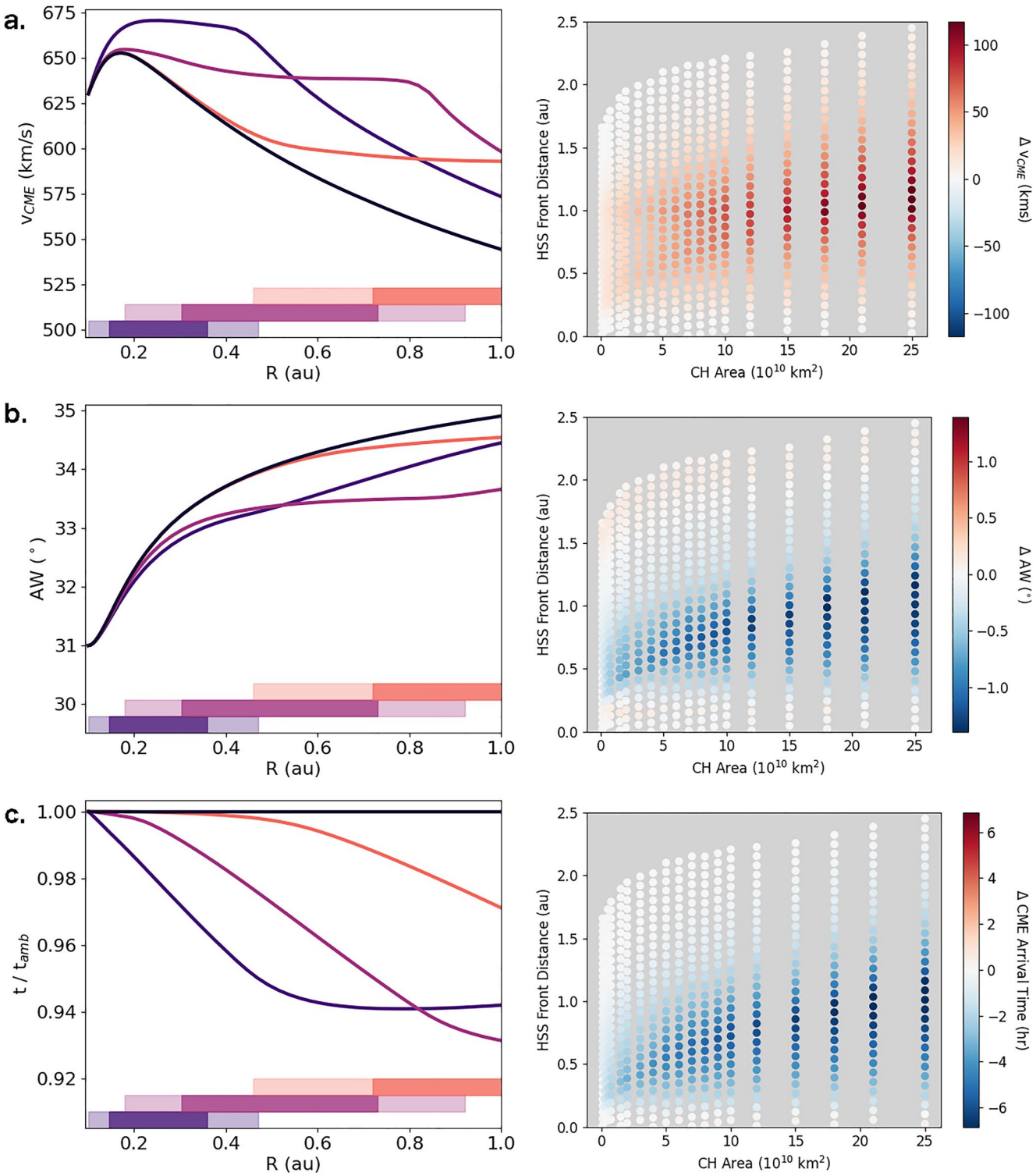

Figure 5. Same as Figure 4 but for the average coronal mass ejection.

indicating increases, blue decreases, and white little to no change. This allows us to visualize what combination of CH area and HSS distance leads to the most significant changes, which sheds light on how CME–HSS interactions affect their impact at Earth. We determine the maximum decrease, Δ_-, and maximum increase, Δ_+, over all ensemble runs, which we list in the last two columns of Tables 2 and 3.

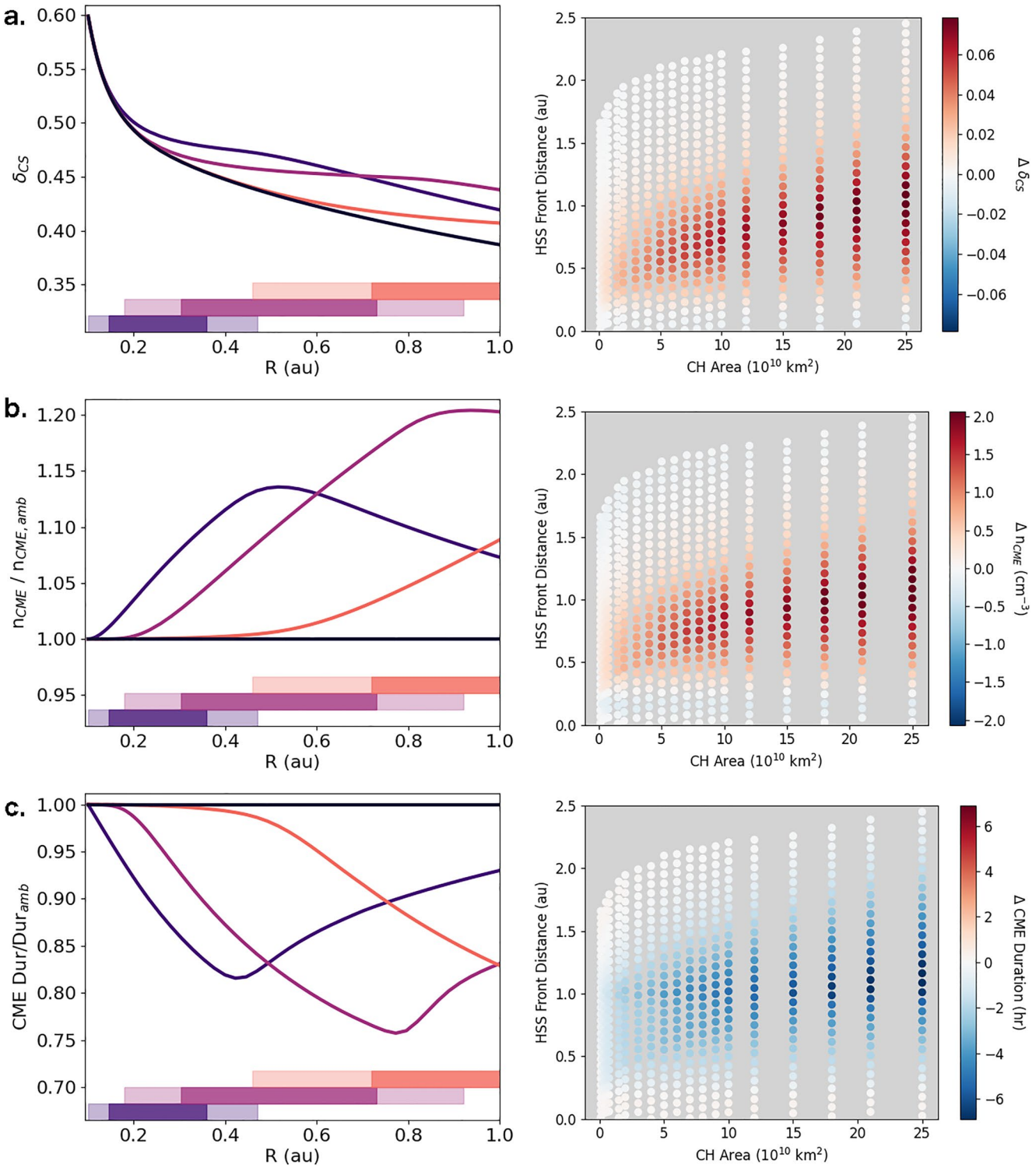

Figure 6. Same as Figure 4 but for the cross-section aspect ratio, the number density of the coronal mass ejection (CME), and the CME duration. For the profiles, the number density is normalized to the ambient case value.

Figure 4 shows (a) the front velocity, (b) the angular width, and (c) the transit time for the fast CME. We see that v_{CME} continually decreases over all distances for the ambient case. When the HSS is close to the Sun, we see a brief initial increase in v_{CME}. This is because the drag force has disappeared but we still have a small outward acceleration from the cross-sectional forces. These accelerating forces only are important for a very short time so

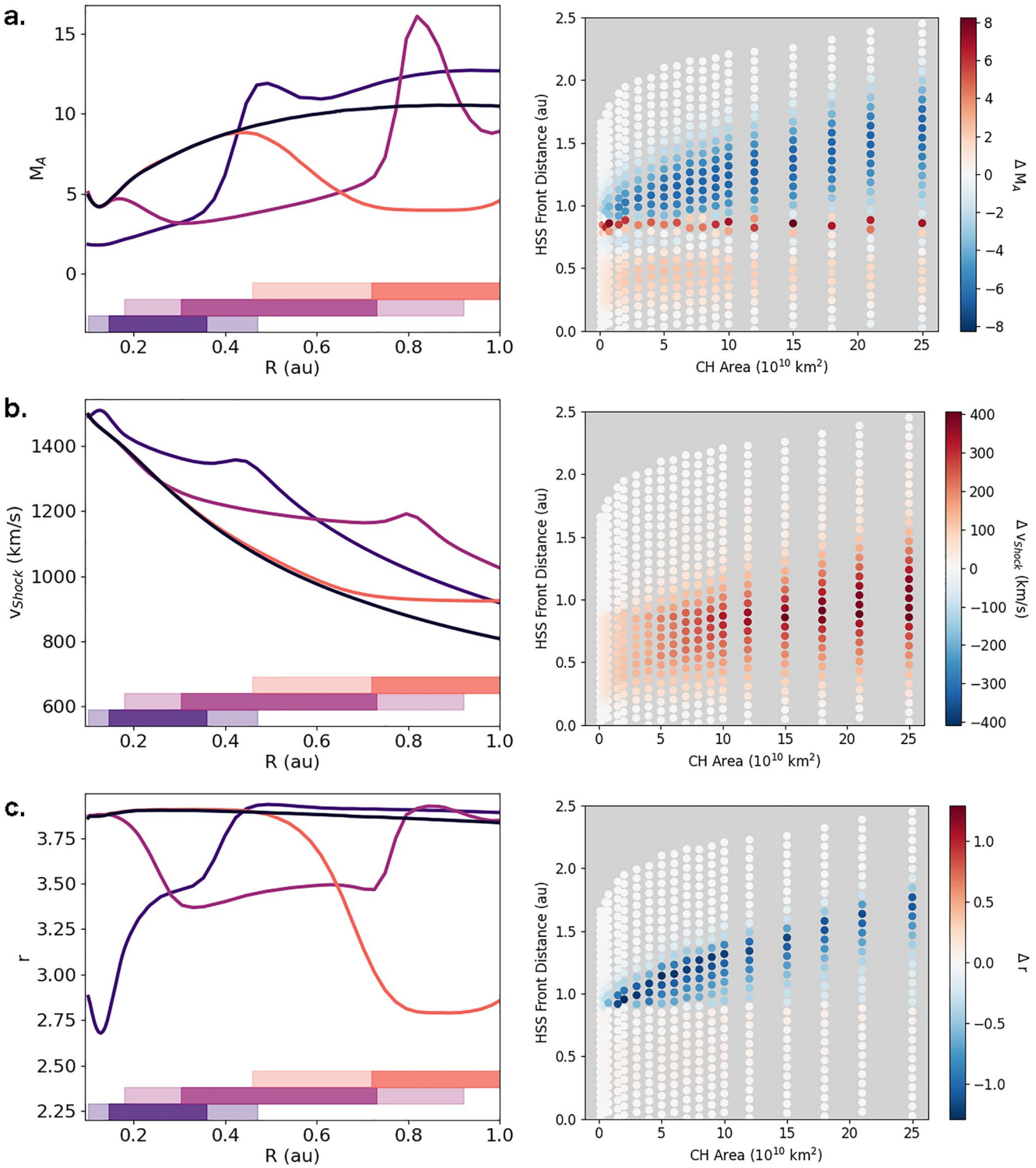

Figure 7. Same as Figure 4 but for the Mach number, the shock speed, and the compression ratio.

v_{CME} begins gradually slowing down by 0.2 au for the two HSS cases with fronts closest to the Sun, followed by a rapid decrease once the CME reaches the SIR. For the other profiles, where the HSS front is at a farther distance, v_{CME} initially decreases at the same rate as the ambient background case, then remains constant while in the HSS plateau, before rapidly decreasing again after. When the interaction occurs closer to the Sun, there is more time

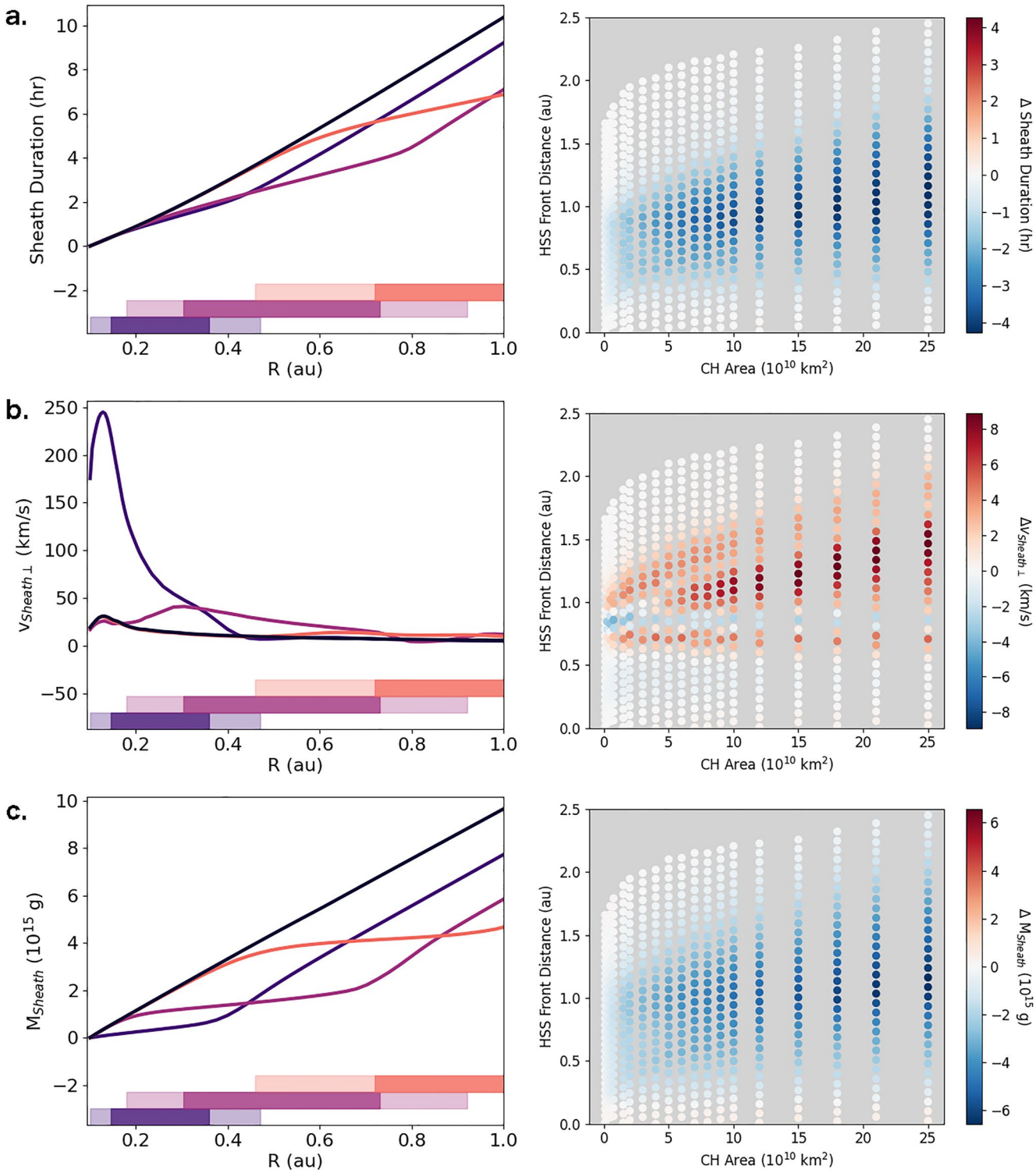

Figure 8. Same as Figure 4 but for the sheath duration, the transverse flow in the sheath, and the sheath mass.

to "recover" after exiting the HSS, so that the profile relaxes toward the ambient case. If the interaction occurs at farther distances, then the majority of the CME's evolution has already occurred and the drag is consequently much weaker because v_{CME} is closer to the solar wind speed. The profiles show that the largest changes in the 1 au value occur for mid-range interactions when the CME exits the HSS right before reaching 1 au.

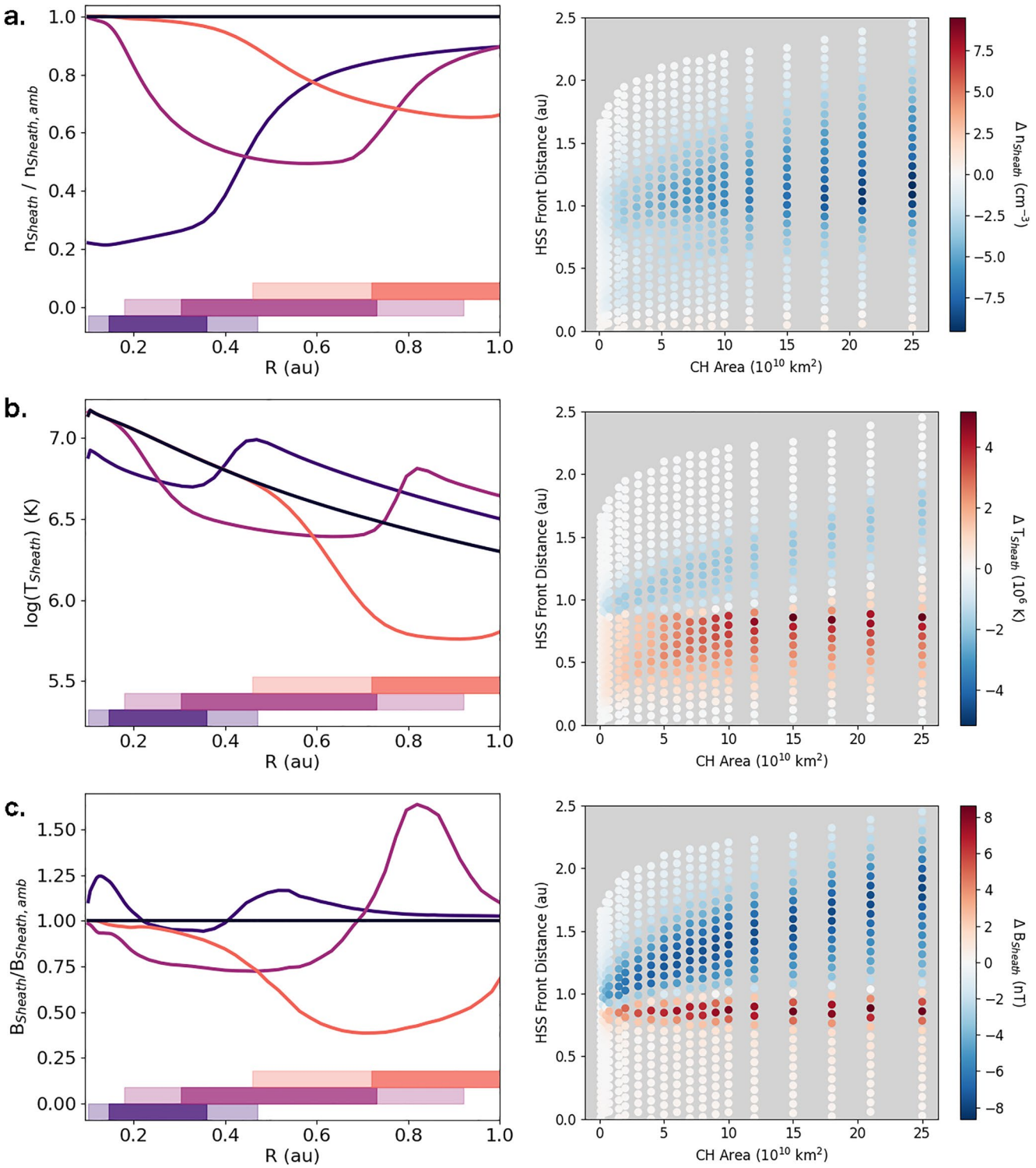

Figure 9. Same as Figure 4 but for the sheath density, the sheath temperature, and the sheath magnetic field strength. The density and magnetic field profiles are shown normalized to the ambient case.

The right panel in Figure 4a shows that this trend is reproduced for any larger CH areas and that the change in the 1 au v_{CME} increases with the CH area. This is as larger CHs produce more extended HSSs, such that the CME spends a longer duration in the low-drag HSS environment. At smaller CH areas, a bifurcation appears for the HSS front distances at which the maximum change occurs. We see a peak for HSS fronts near 1 au, the same the

larger CH areas, and a secondary peak closer to the Sun, hereafter a 1 au peak and a "close" peak. For example, for a CH area of 5×10^{10} km^2, we see peaks near 1 au and 0.6 au. As the CH area decreases, the close peak moves toward 0.4 au. Both of these peaks show much weaker changes than what we see for larger CH areas.

There are two major competing factors that determine the difference in v_{CME} between the HSS case and the 1 au case—(a) how much v_{CME} actually differs while in the HSS and (b) how much time v_{CME} has to recover after. Since the changes in (a) are largely driven by a disappearance of the drag force, this factor will be largest when drag is the highest, which is near the Sun when the velocity differential is the largest. The amount of time to recover is shortest when the CME exits the HSS right before impact. The profiles with smaller CH areas have HSSs with shorter radial extents therefore we see a peak when the HSS is at a location to maximize either one of the two factors. As we consider larger CH areas, we reach a point where the HSS covers the full region between the start of our simulation and 1 au, which causes the two peaks in the maximum change to merge into a single peak right at 1 au. We will find that this pattern appears for many of the output parameters.

The behavior of v_{Exp} (not shown) mirrors that of v_{CME}. v_{Exp} initially increases as the cross section is overpressured relative to the background, but begins decelerating by 0.2 au for all cases. While the CME is within the HSS, v_{CME} is higher, giving the CME expansion less time to decelerate before reaching a given distance, which leads to higher values of v_{Exp}. Once the CME exits the HSS, v_{Exp} approaches the ambient case value. We see the same bifurcation for small CH areas with the peaks corresponding to increases of 10–20 km/s, then a single peak for larger CH areas with increases of 60 km/s for interactions ceasing right before 1 au.

Figure 4b shows that the angular width slowly increases over all distances for all model runs. This is almost entirely driven by the expansion of the cross section due to the initial overpressure, which factors into the full angular extent of the CME. While in the HSS, both v_{CME} and v_{Exp} increase relative to the ambient case, but we find that AW decreases relative to the ambient case, so the effect of having less time to expand must outweigh the increased expansion speed. The final change in AW is small, only decreases of a few degrees. We do not see the bifurcation in the sensitivity for low CH areas. The 1 au peak disappears at low CH areas, so we infer that the early interaction when v_{Exp} is the highest is more dominant than an interaction right before reaching 1 au.

The cross-sectional angular width exhibits the same patterns as the full angular width, so, for brevity, we do not include it in the figures. While in the HSS, $AW_{\perp}$ increases at a slower rate than the ambient case, but gradually recovers after exiting. The change in the final value is about the same as seen for the full AW, a few degrees, but as $AW_{\perp}$ is a much smaller angle, making it a much larger change proportionally.

Figure 4c shows the transit time. For the profiles, we show the transit time to a distance weighted by the corresponding transit time for the ambient case (t/t_{amb}). This makes the ambient case a straight line having a value of one. We see changes up to about 20% of the total transit time to 1 au. The relative time remains at one until the CME enters the tail of the HSS and then quickly drops to lower ratios as the CME propagates faster while in the HSS. The transit time begins recovering upon exiting the HSS, but the effect is far smaller than the recovery we have seen in previous cases. The closer to the Sun that the CME-HSS interaction occurs, the larger the change is in the transit time, provided that the HSS is sufficiently far that the entirety of the HSS plateau is within the simulation domain and not partially below 0.1 au. The right panel shows the 1 au changes in hours and we see that a small HSS causes a decrease of a few hours in the transit time but a large HSS can decrease it by 10 hr.

Figure 5 shows the same parameters as Figure 4, but for the average CME instead of the fast one. There are not any fundamental differences between the fast and average results. We see slightly larger acceleration in v_{CME} due to the cross-sectional expansion, which depends on the initial properties, and again the drag essentially disappears while in the HSS. This causes v_{CME} and v_{Exp} to remain high and the angular widths and transit times to slightly decrease. The magnitude of the changes tends to be slightly smaller for the average case than the fast case since the CME velocity is smaller and thus the drag force weaker. We see the same patterns in the locations where the interaction with the HSS is most effective with the bifurcation appearing for the panel, showing the speed and the early interaction dominating for the angular widths and transit time. As the average CME shows the same trends as the fast case, only with smaller changes, we will only present the results for the fast CME in Figures 6–9.

Figure 6 shows the aspect ratio of (a) the cross section, (b) the density of the CME, and (c) the duration of the CME for the fast CME. For the ambient case, the aspect ratio, δ_{CS}, rapidly decreases until about 0.2 au, then continues to decrease at a slower rate. The HSS causes the CME to experience less pancaking as it reduces the drag force, which tends to be the largest source of deformation as seen in Kay and Nieves-Chinchilla (2021a). The results using a HSS background tend to diverge from the ambient case somewhere between entering the HSS tail and entering the HSS plateau. For the case with the HSS front closest to the Sun, the divergence happens in the plateau, whereas for the case with the farthest HSS front, the divergence is noticeable within the tail. The change in δ_{CS} is most pronounced when the interaction occurs close to the Sun. The CME does recover upon exiting the HSS and relaxes toward the ambient case values. The cross-section aspect ratio changes by 0.2 between 0.1 and 1 au in the ambient case, and the sensitivity plot in the right panel shows that the HSS can reduce the magnitude of the change by 10%–25%. We see nearly identical behavior for the axial aspect ratio (not shown), including the magnitude of the changes.

The profiles Figure 6b show the number density within the CME scaled by the corresponding value for the CME simulated using the ambient background. The sheath density evolves separately and is shown in Figure 9a. As the CME mass stays constant throughout the simulation, the density is essentially a measure of the change in the CME volume. As such, the CME's magnetic field strength and temperature exhibit the same trends as the CME density as they also vary proportionally to the volume. Both AW and $AW_{\perp}$ decrease while within the HSS, which lead to a decrease in the total volume and an increase in the relative density. It begins recovering once the CME exits the SIR. The right panel shows that the CME density can increase by 2 cm^{-3} if the CME interacts with the HSS near 1 au. We also see a region of very slight decreases in the final density when the interaction occurs very close to the Sun. This feature is present but even less noticeable in the sensitivity of v_{CME} in Figure 4b. For these cases, their AW remains nearly constant for between 0.1 and 0.2 au and then slightly increases relative to the ambient case, leading to a minor increase in volume by the time the CME reaches 1 au. While theoretically interesting, this change is very small and nearly indistinguishable from the ambient case.

Figure 6c shows the CME duration relative to the ambient profile. We calculate the shortest path through the nose of the CME and through the center of the cross section, i.e., an impact parameter of zero. The duration will be shorter if a satellite path intersects closer to an edge (larger impact parameter) or longer if it occurs at an oblique angle. The duration depends on both the size and speed of the CME. When the CME enters the HSS, the decreased expansion leads to a shorter path through the CME, which combines with the increase in velocity, causing a decrease in the duration. The profiles mirror that of the density results, but with decreases in the relative values instead of increases. We do see hints of the bifurcation at low CH areas in the sensitivity plot. Interaction with a strong HSS right at 1 au can cause a 7-hr decrease in the duration of a CME, which corresponds to a reduction of about one-third in the duration.

We now consider the evolution of and changes in the sheath properties. We see stronger variation in these properties as many are instantaneous calculations based on the local solar wind properties, rather than parameters evolved over time. This is true of the upstream Alfvénic Mach number, shown in Figure 7a. The Mach number depends on the difference between the CME speed and the solar wind speed and on the Alfvén speed. With our static background, the Alfvén speed varies with radial distance, but it does not change in time due to the passage of the CME and sheath. The Mach number is calculated using the background Alfvén speed immediately upstream of the sheath. The ambient case shows some small variations in the Mach number close to the Sun, followed by a gradual increase at farther distances. For the HSS cases, the Mach number decreases while within the HSS because the velocity differential decreases and the HSS has a higher Alfvén speed as compared to the ambient case. The Mach number peaks when the CME reaches the SIR because the CME speed is still high but the solar wind speed and Alfvén speed begin approaching the ambient values. This leads to a Mach number higher than seen in the ambient case. The Mach number decreases as the background properties continue approaching the ambient values. This quickly reverts to a gradual increase in the Mach number, mirroring the behavior of the ambient case, which results from the velocity differential and Alfvén speed decreasing with distance at slightly different rates. The sensitivity plot shows a nearly horizontal red line just before 1 au, which corresponds to the peak in the profiles when the CME enters the SIR. If the HSS front is farther than 1 au, then the Mach number decreases relative to the ambient case. If the interaction occurs at very

close distances, we find much weaker changes (both positive and negative) as the Mach number approaches the ambient value.

Figure 7b shows the shock speed. For the ambient case, the shock speed continually decreases over time as the speed differential and solar wind speed both decrease. The upstream Mach number decreases once the CME enters the HSS, which can result from changes in the upstream Alfvén speed or the upstream speed, which is the difference between the shock speed and the solar wind speed. The Alfvén speed increases in the HSS and the closer analysis shows that the upstream speed decreases. Since the shock speed increases while the CME is within the HSS, the increase in the background solar wind speed must outweigh the decrease in the upstream speed. We see a local peak in the shock speed within the SIR but the shock speed rapidly begins recovering immediately after. The backgrounds corresponding to the largest CH areas can produce increases of more than 400 km/s in the 1 au shock velocity, equivalent to a change of 48%.

Figure 7c shows the compression ratio. The ambient case has a constant compression of around 3.85, which is not significantly less than the theoretical limit of four (Priest, 1982). As this is an instantaneous calculation, the compression immediately drops when the CME enters the HSS tail. For most cases, we have a nearly constant compression within the HSS plateau, which then returns to the ambient case values upon exit. The compression while in the HSS plateau is smaller for farther HSS fronts. For the profiles with the HSS front closest to the Sun, we see the compression decrease to lower values in the HSS tail than within the HSS plateau. In the sensitivity panel, the changes from the ambient case are largest when the CME enters the HSS plateau at 1 au.

Figure 8a shows the duration of the CME-driven sheath. The width begins at zero and slowly increases over time with the ambient case having a 1 au duration of 8.7 hr. When the CME is in the HSS, the shock speed is higher but the CME speed is also higher. This results in a smaller speed difference between the CME and the shock so that the duration of the CME increases less while it is in the HSS. Once the CME exits the HSS, both the shock and CME speeds start decreasing but the sheath duration approaches the ambient profile. In the sensitivity panel, we see a fairly wide range in which distances produce meaningful effects. A strong HSS can produce a change of 4 hr in the duration, which represents a decrease of 50%.

We also consider the arrival time of the sheath (not shown). This corresponds to the arrival time of the CME front plus the sheath duration. The results mimic the CME arrival time figures. We see that the most significant decreases in the transit time when the interaction ceases right before 1 au.

Figure 8b shows the lateral flow in the sheath. For the majority of cases, the flow is very slow, typically less than 20 km/s. However, when the CME interacts with the HSS close to the sun, we find large deviations from the ambient case. In this regime, we have a very high Alfvén speed (>200 km/s), allowing for fast lateral flows, which prevent a strong shock from forming. The sensitivity panel shows the inverse of the behavior for the Mach number. We observe a decrease in flows right when the CME exits the HSS at 1 au. When the HSS front is farther and the CME is embedded in the HSS at 1 au, the lateral flows increase by 5–10 km/s because of the higher Alfvén speed.

Figure 8c shows the sheath mass, which mimics the behavior of the sheath duration, only with more noticeable changes. The upstream speed decreases while the CME is in the HSS and the material flows into the downstream region at a slower rate. The HSS has lower number density that the ambient case, which further contributes to the sheath mass growing at a much slower rate while in the HSS. At the center of the SIR, the sheath mass begins growing at a rate slightly faster than the ambient case. In the sensitivity panel, we see some evidence of the bifurcation at small CH areas. We also see that a wider range of distances produce significant changes for backgrounds with larger CH areas. This results from the sheath mass immediately deviating from the ambient case values so we see a large change if the CME is at any distance within the HSS. Interaction with the HSS can decrease the sheath mass by 81%.

Figure 9 shows the density, temperature, and magnetic field within the sheath. Unlike within the CME, these do not evolve proportional to the same volume, rather they are outputs of the shock model. Figure 9a shows the sheath density relative to the sheath density in the ambient case, which evolves based on the sheath mass and the sheath volume. The sheath mass grows at a slower rate while in the HSS. The volume is the product of the CME's angular width and the sheath's radial width, both of which decrease relative to the ambient case while in the HSS. We find that the sheath density decreases so the relative decrease in the mass is more effective than the relative

decrease in volume. The percentage change is largest when the interaction occurs close to the Sun with as much as an 80% decrease in the sheath density, but it quickly begins recovering after exiting the HSS plateau. Interactions at farther distances can still cause a 35% change in the sheath density. The sensitivity panel shows the highest sensitivity to interactions where the CME is within the HSS plateau, which can lead to decreases of 9.5 cm^{-3} in the sheath density at 1 au. We see some hints of the bifurcated structure for small CH areas. For the small CH area cases, the changes are much weaker when the interaction occurs close to the Sun rather than near 1 au.

Figure 9b shows the sheath temperature, which is calculated instantaneously from the shock solution and the solar wind temperature, making it highly variable like the Mach number and transverse flow. The ambient sheath temperature decreases with distance but is one to two orders of magnitude higher than the background solar wind temperature. The solar wind temperature is higher within the HSS than the ambient solar wind, but the CME also drives a weaker shock, resulting in less heating of the sheath in the HSS plateau. Once the CME exits the HSS plateau, the shock strength abruptly increases, causing the sheath temperature to exceed that of the ambient case. As propagation continues, the sheath temperature declines. The sensitivity plot shows that this trend extends to all CH areas, and we see less of a difference between small and large areas than seen for most other parameters. The fast CME has a 1 au sheath temperature around 2.5 MK. Interactions close to the Sun with the CME exiting right before 1 au tend to cause an increase of 2 MK in the sheath temperature though we see a few cases with an increase of up to 5 MK. When the CME is embedded in the plateau at 1 au, we find decreases up to 2 MK. We remind that we expect these values to be reasonable for the sheath region immediately adjacent to the shock, but a more sophisticated model is needed for the sheath temperatures farther from the shock, as it should consider how structures evolve within the sheath due the continuous addition of materials from the pileup process.

Figure 9c shows the relative magnetic field strength within the sheath, which, like the temperature, is calculated instantaneously and assumed to apply to the entire uniform sheath. The background magnetic field is stronger in the HSS but the shock is weaker, so we ultimately see weaker sheath magnetic field while in the sheath. The relative decrease is largest right when the CME leaves the HSS tail and enters the plateau, which is where the shock is the weakest. The change is largest for interactions farthest from the Sun with the orange profile showing a decrease of roughly 70% in the sheath magnetic field. Upon exiting the HSS plateau, the sheath magnetic field strength peaks beyond the SIR. For the profile with the closest HSS front, we see a brief enhancement in the sheath magnetic field at the closest distances. This is the same region where we saw the enhancement in the lateral flow. The sensitivity panel is similar to the temperature sensitivity panel, but with a smaller range of distances causing increases in the sheath magnetic field. The profiles show that the magnetic field recovers fairly quickly so an enhancement would only be observed if the CME has recently exited the HSS. Interaction with an HSS can cause the sheath magnetic field to change by ±8 nT, and weaker HSS can cause nearly as extreme changes as stronger HSS.

7. Discussion

A major goal of this paper is to explore whether there is a critical distance where the interaction between a CME and HSS is the "most important," or at least consistently produces the largest changes in the properties of a CME and its sheath at 1 au. Throughout Section 6, we found that the most important interactions happen either close to the Sun, when the velocity differential between the CME and background solar wind is the highest, or farther out, such that the CME spends a long time within the HSS and exits it right before reaching 1 au, leaving no time for recovery. For smaller HSSs, these two critical points correspond to different distances of the HSS front. As the HSS size increases, the two distinct distances merge into one once the HSS width has become sufficiently long to simultaneously maximize both criteria.

We also found that there are different regions within the HSS that are the most important for different CME parameters. All of the CME parameters, as well as the sheath compression, duration, transverse flow, mass, and density, show the largest changes during passage through the HSS tail and the plateau. Typically, the change is largest right before exiting the plateau as it represents the accumulated changes over the full tail and the plateau. The shock speed, sheath temperature, and sheath magnetic field strength exhibit the largest changes in the SIR. These are the properties that are determined instantaneously based on the local solar wind background rather than evolving over the full propagation. For a real sheath, this will not instantaneously change the temperature and magnetic field strength of the entire sheath, this is an oversimplification of our model. However, interaction

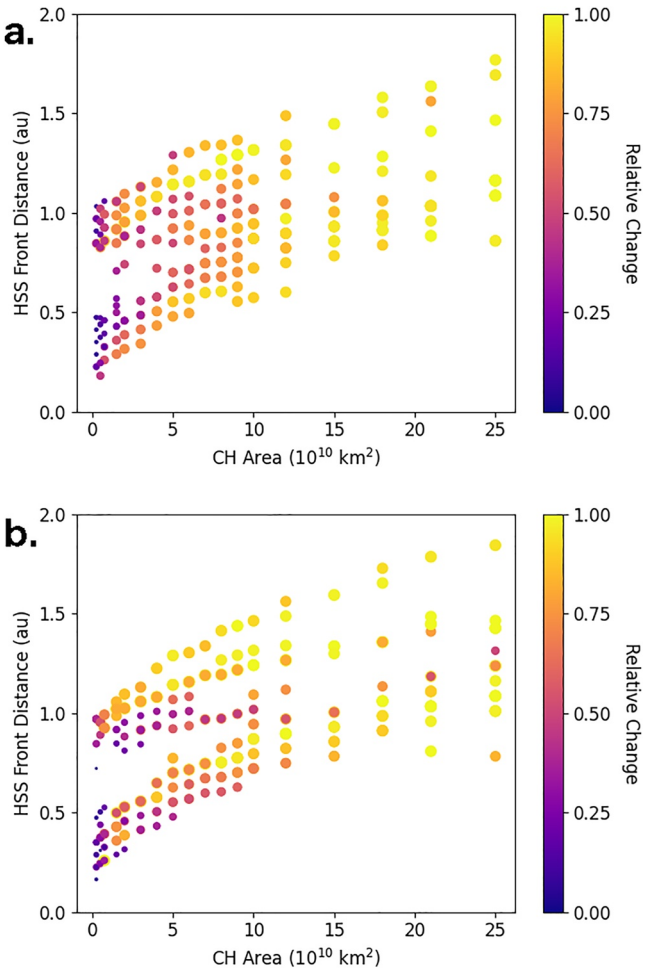

Figure 10. High-speed stream (HSS) distance corresponding to the maximum change in each parameter for each CH area. The individual dots are weighted by the maximum change in that parameter across all CH sizes and HSS distances. Small, purple circles indicate a small relative change, whereas large, yellow circles represent near the maximum change in that parameter. Panel (a) shows results for the fast coronal mass ejection (CME) and panel (b) shows results for the average CME.

with a SIR should still produce the maximum changes in the temperature and magnetic field at front of the sheath near the shock.

To further explore these trends, for each CME and sheath parameter, and for each CH area, we determine the HSS front distance, which produces the largest change, positive or negative, in that parameter at 1 au. We then have 23 measurements, corresponding to the 23 parameters, of the "most important" distance for each CH area. Figure 10 shows a scatterplot of these 23 distances for each CH area. We note that many of the points overlap and cannot be individually distinguished as we are considering discrete distances, determined by our 6 hr time sampling of the MHD results. For each parameter, we determine the maximum unsigned change in it over all CH areas, which typically occurs for the largest CH area. We define a relative importance as the change in a parameter at a given CH area divided by the maximum change in that parameter over all CH areas. In Figure 10, we scale both the symbol size and color of each distance using the relative importance, with larger, brighter points being more important.

The scatterplots reproduce the bifurcated structure in the critical distance for weaker HSSs. The effect is slightly more noticeable for the average CME (10(b)) than the fast one (10(a)). The critical distances are almost evenly split between close and near 1 au critical distances at small CH areas. We find a slight preference for 1 au for the fast CME and close distances for the average CME, but caution the statistical significance of these results without further investigation.

We confirm that the largest changes occur for the strongest HSS. We see a few examples for the average CME where the largest HSS does not have the most extreme changes for a few parameters. There are also many cases where moderate strength HSS produces nearly as much of a change as the largest HSS. These yellow points tend to extend backward until about the CH area where the bifurcation appears (about 7 times 10^{10} km^2). This suggests that if the HSS is large enough, the drag on a CME is negligible for most of the CME's propagation and a stronger impact will be seen at 1 au as compared to the ambient background case. This is not exactly a groundbreaking revelation, one might expect such from common sense intuition, but it shows that the exact sizes of the HSS plateau, tail, and SIR do not significantly affect the sheath and CME parameters at 1 au.

The primary effect of the HSS appears to be eliminating the drag force that decelerates a CME within the ambient solar wind background. In theory, the drag force causes the CME to accelerate while within the HSS, but the HSS density is relatively low leading to an ineffective acceleration. This suggests that if drag is no longer significantly effecting a CME that it is already at the solar wind speed, that interaction with a HSS will have little to no effect on the CME. Using our empMHD background, we estimate that the fast CME reaches the ambient background speed around 5–8 au and the average CME around 2–5 au, depending on how precisely one requires the match to be. We do not have background profiles with HSS at these distances so we cannot test this speculation, it remains an interesting theory. We also note that beyond 1 au, HSS evolves into corotating interaction regions, potentially with forward and reverse shocks, so the assumption of simply faster speed and weaker density may be an oversimplification.

The ability to incorporate an HSS into the solar wind background could be important for space weather predictions at Earth. We find a ten-hour difference in the CME arrival time, which is around the current uncertainty in arrival time predictions. It is difficult to assess which changes are the most "important" without some standardized measures quantifying the response of a geomagnetic storm to a change in velocity versus magnetic field versus density and so on. Looking at the magnitude of our changes, the CME velocity immediately jumps out as

intuitively feeling like a much larger magnitude change than the other parameters. We have frequently used the expression

$$Kp = 9.5 - \exp\left[2.17676 - 0.000052 v^{4/3} B_t^{2/3} \sin^{8/3}\frac{\theta_C}{2}\right] \quad (18)$$

to estimate the Kp index from the velocity, v (in km/s), and tangential magnetic field strength (in nT), B_t, which is at a clock angle θ_C in GSE coordinates. If we make the assumption that v is v_{CME} and that B_t is the tangential sheath field $B_{\text{Sheath}} \sin\theta_{\text{Sheath}}$ is at a θ_C of 45°, then we would expect a Kp of 5.44 for the sheath. An increase of 379 km/s, which is the maximum increase in CME velocity we found, would increase the Kp to 7.29. An increase of B_{Sheath} by 8.6 nT, the maximum we found, would only increase the Kp to 6.38. We determine an even larger Kp of 8.12 if we consider simultaneous changes in the velocity and magnetic field. Accounting for this, the magnitude of changes in Kp is certainly important for any space weather predictions.

Finally, we note that we have assumed a static HSS background. Real (and MHD) HSSs propagate and evolve in time instead of remaining fixed in space. If the CME speed matches that of the HSS, their interaction can be prolonged for greater distances than seen in the static cases. Alternatively, a slow CME can be pushed by an HSS from behind. Both of these dynamic situations will lead to more extreme changes in the CME and sheath properties. Future work will incorporate time dependence into our HSS background and quantify these effects.

8. Conclusion

We presented a new model for the formation of a CME-driven sheath within a simplified, analytic arrival time model. Using the Rankine-Hugoniot relations, we can study the shock that forms based on the CME and background solar wind properties and simulate the accumulation of materials into a sheath region.

We have adapted our model to use a one-dimensional profile for the background solar wind, rather than relying on a simplistic empirical model, as was used in previous studies. We show that for an ambient solar wind background, the results do not fundamentally change between using a background profile from an MHD model and using the previous empirical model, provided that the empirical model is tuned to match the MHD value at 1 au. We then replaced the ambient MHD background with a profile from an MHD simulation including an HSS. We determined how the evolution of the CME and the sheath changes when the CME interacts with the HSS instead of the ambient background. We find that the drag force approaches zero while the CME is within the HSS, but reappears stronger once it exits.

We have extended our analysis to different-size HSSs at different distances. We sought to understand at what distance does the CME-HSS interaction cause the largest changes in the final properties at 1 au. We find that two critical distances occur: (a) close to the Sun when the CME has the highest speed or (b) close to 1 au such that the CME stops interacting with the HSS right before impact. For smaller HSSs, the two cases correspond to two distinct distances of the HSS front. As the HSS grows, it reaches a point where the front can be situated near 1 au but the full structure extends back toward the Sun far enough to affect the initial evolution of the CME as well. The magnitude of the changes in CME and sheath properties, relative to the ambient case, increases with HSS size until the HSS is sufficiently large to cover this full distance, at which any changes remain relatively constant, at least for the MHD profiles used in this work.

These results have significant implication for space weather forecasting. Interactions with an HSS reduce the drag on a fast CME, leading to faster speeds and shorter transit times. Our results show that the interaction can cause the transit time to decrease by 10 hr, a reduction of 25%. The interaction with an HSS can also result in significant changes in the geoeffectiveness of a CME, and in particular in the CME-driven sheath. We estimated a Kp index of 5.44 resulting from the impact of an example fast CME in a steady-state background. Interaction with a large HSS could cause the Kp to increase to 8.12, which represents a significantly more severe geomagnetic storm, for which an accurate forecast would be critical.

Finally, it is clear from the results presented in this work that a full characterization of the ambient solar wind through which a CME propagates is crucial for a more accurate determination of its internal properties and geoeffectiveness. In the context of MHD modeling, several works have focused on the validation of simulation outputs in comparison to in situ observations (e.g., Lee et al., 2009; Gonzi et al., 2021; Gressl et al., 2014; Hinterreiter

et al., 2019; Samara et al., 2021). These studies have found, for example, that results can differ more or less dramatically depending on the coronal model and input magnetogram(s) that are considered, and that predicted HSS arrival times have typical uncertainties of the order of about 1 day. Future improvements in this direction will not only provide more accurate forecasts of the large-scale structure of the solar wind, but also of the impact of CMEs that propagate through it.

Data Availability Statement

The OSPREI model, including ANTEATR, is publicly available at github.com/ckay314/OSPREI. The version of ANTEATR-PUP used for this paper is archived through Zenodo at https://doi.org/10.5281/zenodo.6828805.

Acknowledgments
C. Kay is supported by the National Aeronautics and Space Administration under Grant 80NSSC19K0274 issued through the Heliophysics Guest Investigators Program and Grant 80NSSC19K0909 issued through the Heliophysics Early Career Investigators Program. C. Kay and E. Palmerio acknowledge support from NASA PSP-GI Grant No. 80NSSC22K0349. S. J. Hofmeister acknowledges support by the DFG Grant 448336908. E. Palmerio also acknowledges NASA HTMS Grant No. 80NSSC20K1274.

References

Barnard, L., Owens, M. J., Scott, C. J., Lockwood, M., de Koning, C. A., Amerstorfer, T., et al. (2022). Quantifying the uncertainty in CME kinematics derived from geometric modeling of heliospheric imager data. *Space Weather*, *20*(1), e2021SW002841. https://doi.org/10.1029/2021SW002841

Berdichevsky, D. B., Richardson, I. G., Lepping, R. P., & Martin, S. F. (2005). On the origin and configuration of the 20 March 2003 interplanetary shock and magnetic cloud at 1 AU. *Journal of Geophysical Research*, *110*(A9), A09105. https://doi.org/10.1029/2004JA010662

Cane, H. V., & Richardson, I. G. (2003). Interplanetary coronal mass ejections in the near-Earth solar wind during 1996–2002. *Journal of Geophysical Research*, *108*(A4), 1156. https://doi.org/10.1029/2002JA009817

Davies, E. E., Möstl, C., Owens, M. J., Weiss, A. J., Amerstorfer, T., Hinterreiter, J., et al. (2021). In situ multi-spacecraft and remote imaging observations of the first CME detected by Solar Orbiter and BepiColombo. *Astronomy & Astrophysics*, *656*, A2. https://doi.org/10.1051/0004-6361/202040113

Durand-Manterola, H. J., Flandes, A., Rivera, A. L., Lara, A., & Niembro, T. (2017). CMEs' speed, travel time, and temperature: A thermodynamic approach. *Journal of Geophysical Research: Space Physics*, *122*(12), 11845–11856. https://doi.org/10.1002/2017JA024369

Gonzalez, W. D., & Tsurutani, B. T. (1987). Criteria of interplanetary parameters causing intense magnetic storms ($D_{st} < -100$ nT). *Planetary and Space Science*, *35*(9), 1101–1109. https://doi.org/10.1016/0032-0633(87)90015-8

Gonzalez, W. D., Tsurutani, B. T., & Clúa de Gonzalez, A. L. (1999). Interplanetary origin of geomagnetic storms. *Space Science Reviews*, *88*(3/4), 529–562. https://doi.org/10.1023/A:1005160129098

Gonzi, S., Weinzierl, M., Bocquet, F. X., Bisi, M. M., Odstrcil, D., Jackson, B. V., et al. (2021). Impact of inner heliospheric boundary conditions on solar wind predictions at Earth. *Space Weather*, *19*(1), e2020SW002499. https://doi.org/10.1029/2020SW002499

Gopalswamy, N., Lara, A., Yashiro, S., Kaiser, M. L., & Howard, R. A. (2001). Predicting the 1-AU arrival times of coronal mass ejections. *Journal of Geophysical Research*, *106*(A12), 29207–29218. https://doi.org/10.1029/2001JA000177

Gressl, C., Veronig, A. M., Temmer, M., Odstrčil, D., Linker, J. A., Mikić, Z., & Riley, P. (2014). Comparative study of MHD modeling of the background solar wind. *Solar Physics*, *289*(5), 1783–1801. https://doi.org/10.1007/s11207-013-0421-6

Heinemann, S. G., Temmer, M., Farrugia, C. J., Dissauer, K., Kay, C., Wiegelmann, T., et al. (2019). CME-HSS interaction and characteristics tracked from Sun to Earth. *Solar Physics*, *294*(9), 121. https://doi.org/10.1007/s11207-019-1515-6

Hellinger, P., TráVníček, P. M., Štverák, Š., Matteini, L., & Velli, M. (2013). Proton thermal energetics in the solar wind: Helios reloaded. *Journal of Geophysical Research*, *118*(4), 1351–1365. https://doi.org/10.1002/jgra.50107

Hinterreiter, J., Amerstorfer, T., Temmer, M., Reiss, M. A., Weiss, A. J., Möstl, C., et al. (2021). Drag-based CME modeling with heliospheric images incorporating frontal deformation: ELEvoHI 2.0. *Space Weather*, *19*(10), e2021SW002836. https://doi.org/10.1029/2021SW002836

Hinterreiter, J., Magdalenic, J., Temmer, M., Verbeke, C., Jebaraj, I. C., Samara, E., et al. (2019). Assessing the performance of EUHFORIA modeling the background solar wind. *Solar Physics*, *294*(12), 170. https://doi.org/10.1007/s11207-019-1558-8

Hofmeister, S. J., Veronig, A. M., Poedts, S., Samara, E., & Magdalenic, J. (2020). On the dependency between the peak velocity of high-speed solar wind streams near Earth and the area of their solar source coronal holes. *The Astrophysical Journal Letters*, *897*(1), L17. https://doi.org/10.3847/2041-8213/ab9d19

Janvier, M., Démoulin, P., & Dasso, S. (2013). Global axis shape of magnetic clouds deduced from the distribution of their local axis orientation. *Astronomy and Astrophysics*, *556*, A50. https://doi.org/10.1051/0004-6361/201321442

Jian, L., Russell, C. T., Luhmann, J. G., & Skoug, R. M. (2006). Properties of interplanetary coronal mass ejections at one AU during 1995–2004. *Solar Physics*, *239*(1–2), 393–436. https://doi.org/10.1007/s11207-006-0133-2

Jin, M., Manchester, W. B., van der Holst, B., Sokolov, I., Tóth, G., Vourlidas, A., et al. (2017). Chromosphere to 1 AU simulation of the 2011 March 7th event: A comprehensive study of coronal mass ejection propagation. *The Astrophysical Journal*, *834*(2), 172. https://doi.org/10.3847/1538-4357/834/2/172

Kay, C., & Gopalswamy, N. (2018). The effects of uncertainty in initial CME input parameters on deflection, rotation, B_z, and arrival time predictions. *Journal of Geophysical Research*, *123*(9), 7220–7240. https://doi.org/10.1029/2018JA025780

Kay, C., Gopalswamy, N., Reinard, A., & Opher, M. (2017). Predicting the magnetic field of Earth-impacting CMEs. *The Astrophysical Journal*, *835*(2), 117. https://doi.org/10.3847/1538-4357/835/2/117

Kay, C., Mays, M. L., & Collado-Vega, Y. M. (2022). OSPREI: A coupled approach to modeling CME-driven space weather with automatically generated, user-friendly outputs. *Space Weather*, *20*(4), e02914. https://doi.org/10.1029/2021SW002914

Kay, C., Mays, M. L., & Verbeke, C. (2020). Identifying critical input parameters for improving drag-based CME arrival time predictions. *Space Weather*, *18*(1), e2019SW002382. https://doi.org/10.1029/2019SW002382

Kay, C., & Nieves-Chinchilla, T. (2021a). Modeling interplanetary expansion and deformation of CMEs with ANTEATR PARADE: Relative contribution of different forces. *Journal of Geophysical Research*, *126*(5), e2020JA028911. https://doi.org/10.1029/2020JA028911

Kay, C., & Nieves-Chinchilla, T. (2021b). Modeling interplanetary expansion and deformation of coronal mass ejections with ANTEATR-PARADE: Sensitivity to input parameters. *Journal of Geophysical Research*, *126*(6), e2020JA028966. https://doi.org/10.1029/2020JA028966

Kay, C., Nieves-Chinchilla, T., & Jian, L. K. (2020). FIDO-SIT: The first forward model for the in situ magnetic field of CME-driven sheaths. *Journal of Geophysical Research*, *125*(2), e2019JA027423. https://doi.org/10.1029/2019JA027423

Kay, C., Opher, M., & Evans, R. M. (2015). Global trends of CME deflections based on CME and solar parameters. *The Astrophysical Journal*, *805*(2), 168. https://doi.org/10.1088/0004-637X/805/2/168

Kilpua, E. K. J., Fontaine, D., Moissard, C., Ala-Lahti, M., Palmerio, E., Yordanova, E., et al. (2019). Solar wind properties and geospace impact of coronal mass ejection-driven sheath regions: Variation and driver dependence. *Space Weather*, *17*(8), 1257–1280. https://doi.org/10.1029/2019SW002217

Kilpua, E. K. J., Good, S. W., Palmerio, E., Asvestari, E., Lumme, E., Ala-Lahti, M., et al. (2019). Multipoint observations of the June 2012 interacting interplanetary flux ropes. *Frontiers in Astronomy and Space Sciences*, *6*, 50. https://doi.org/10.3389/fspas.2019.00050

Kilpua, E. K. J., Koskinen, H. E. J., & Pulkkinen, T. I. (2017). Coronal mass ejections and their sheath regions in interplanetary space. *Living Reviews in Solar Physics*, *14*(1), 5. https://doi.org/10.1007/s41116-017-0009-6

Kumar, A., & Rust, D. M. (1996). Interplanetary magnetic clouds, helicity conservation, and current-core flux-ropes. *Journal of Geophysical Research*, *101*(A7), 15667–15684. https://doi.org/10.1029/96JA00544

Kunkel, V., & Chen, J. (2010). Evolution of a coronal mass ejection and its magnetic field in interplanetary space. *The Astrophysical Journal Letters*, *715*(2), L80–L83. https://doi.org/10.1088/2041-8205/715/2/L80

Lee, C. O., Luhmann, J. G., Odstrcil, D., MacNeice, P. J., de Pater, I., Riley, P., & Arge, C. N. (2009). The solar wind at 1 AU during the declining phase of solar cycle 23: Comparison of 3D numerical model results with observations. *Solar Physics*, *254*(1), 155–183. https://doi.org/10.1007/s11207-008-9280-y

Liu, J., Ye, Y., Shen, C., Wang, Y., & Erdélyi, R. (2018). A new tool for CME arrival time prediction using machine learning algorithms: CAT-PUMA. *The Astrophysical Journal*, *855*(2), 109. https://doi.org/10.3847/1538-4357/aaae69

Lugaz, N., Farrugia, C. J., Winslow, R. M., Al-Haddad, N., Kilpua, E. K. J., & Riley, P. (2016). Factors affecting the geoeffectiveness of shocks and sheaths at 1 AU. *Journal of Geophysical Research: Space Physics*, *121*(11), 10861–10879. https://doi.org/10.1002/2016JA023100

Mishra, W., & Wang, Y. (2018). Modeling the thermodynamic evolution of coronal mass ejections using their kinematics. *The Astrophysical Journal*, *865*(1), 50. https://doi.org/10.3847/1538-4357/aadb9b

Möstl, C., Rollett, T., Frahm, R. A., Liu, Y. D., Long, D. M., Colaninno, R. C., et al. (2015). Strong coronal channelling and interplanetary evolution of a solar storm up to Earth and Mars. *Nature Communications*, *6*(1), 7135. https://doi.org/10.1038/ncomms8135

Nieves-Chinchilla, T., Alzate, N., Cremades, H., Rodriguez-Garcia, L., Dos Santos, L. F. G., Narock, A., et al. (2022). Direct first Parker Solar Probe Observation of the interaction of two successive interplanetary coronal mass ejections in 2020 November. *The Astrophysical Journal*, *930*(1), 88. https://doi.org/10.3847/1538-4357/ac590b

Nieves-Chinchilla, T., Linton, M. G., Hidalgo, M. A., & Vourlidas, A. (2018). Elliptic-cylindrical analytical flux rope model for magnetic clouds. *The Astrophysical Journal*, *861*(2), 139. https://doi.org/10.3847/1538-4357/aac951

Odstrcil, D., Pizzo, V. J., Linker, J. A., Riley, P., Lionello, R., & Mikic, Z. (2004). Initial coupling of coronal and heliospheric numerical magnetohydrodynamic codes. *Journal of Atmospheric and Solar-Terrestrial Physics*, *66*(15–16), 1311–1320. https://doi.org/10.1016/j.jastp.2004.04.007

Owens, M., & Cargill, P. (2004). Non-radial solar wind flows induced by the motion of interplanetary coronal mass ejections. *Annales Geophysicae*, *22*(12), 4397–4406. https://doi.org/10.5194/angeo-22-4397-2004

Palmerio, E., Kay, C., Al-Haddad, N., Lynch, B. J., Yu, W., Stevens, M. L., et al. (2021). Predicting the magnetic fields of a stealth CME detected by Parker Solar Probe at 0.5 au. *The Astrophysical Journal*, *920*(2), 65. https://doi.org/10.3847/1538-4357/ac25f4

Palmerio, E., Nieves-Chinchilla, T., Kilpua, E. K. J., Barnes, D., Zhukov, A. N., Jian, L. K., et al. (2021). Magnetic structure and propagation of two interacting CMEs from the Sun to Saturn. *Journal of Geophysical Research: Space Physics*, *126*(11), e2021JA029770. https://doi.org/10.1029/2021JA029770

Paouris, E., & Mavromichalaki, H. (2017). Effective acceleration model for the arrival time of interplanetary shocks driven by coronal mass ejections. *Solar Physics*, *292*(12), 180. https://doi.org/10.1007/s11207-017-1212-2

Pomoell, J., & Poedts, S. (2018). EUHFORIA: European heliospheric forecasting information asset. *Journal of Space Weather and Space Climate*, *8*, A35. https://doi.org/10.1051/swsc/2018020

Priest, E. R. (1982). Solar magneto-hydrodynamics.

Pulkkinen, T. (2007). Space weather: Terrestrial perspective. *Living Reviews in Solar Physics*, *4*(1), 1. https://doi.org/10.12942/lrsp-2007-1

Riley, P., & Crooker, N. U. (2004). Kinematic treatment of coronal mass ejection evolution in the solar wind. *The Astrophysical Journal*, *600*(2), 1035–1042. https://doi.org/10.1086/379974

Russell, C. T., & Mulligan, T. (2002). On the magnetosheath thicknesses of interplanetary coronal mass ejections. *Planetary and Space Sciences*, *50*(5–6), 527–534. https://doi.org/10.1016/S0032-0633(02)00031-4

Samara, E., Pinto, R. F., Magdalenić, J., Wijsen, N., Jerčić, V., Scolini, C., et al. (2021). Implementing the MULTI-VP coronal model in EUHFORIA: Test case results and comparisons with the WSA coronal model. *Astronomy & Astrophysics*, *648*, A35. https://doi.org/10.1051/0004-6361/202039325

Savani, N. P., Owens, M. J., Rouillard, A. P., Forsyth, R. J., & Davies, J. A. (2010). Observational evidence of a coronal mass ejection distortion directly attributable to a structured solar wind. *The Astrophysical Journal Letters*, *714*(1), L128–L132. https://doi.org/10.1088/2041-8205/714/1/L128

Savani, N. P., Vourlidas, A., Szabo, A., Mays, M. L., Richardson, I. G., Thompson, B. J., et al. (2015). Predicting the magnetic vectors within coronal mass ejections arriving at Earth: 1. Initial architecture. *Space Weather*, *13*(6), 374–385. https://doi.org/10.1002/2015SW001171

Scolini, C., Chané, E., Temmer, M., Kilpua, E. K. J., Dissauer, K., Veronig, A. M., et al. (2020). CME-CME interactions as sources of CME geoeffectiveness: The formation of the complex ejecta and intense geomagnetic storm in 2017 early September. *The Astrophysical Journal - Supplement Series*, *247*(1), 21. https://doi.org/10.3847/1538-4365/ab6216

Shen, C., Xu, M., Wang, Y., Chi, Y., & Luo, B. (2018). Why the shock-ICME complex structure is important: Learning from the early 2017 September CMEs. *The Astrophysical Journal*, *861*(1), 28. https://doi.org/10.3847/1538-4357/aac204

Shi, T., Wang, Y., Wan, L., Cheng, X., Ding, M., & Zhang, J. (2015). Predicting the arrival time of coronal mass ejections with the graduated cylindrical shell and drag force model. *The Astrophysical Journal*, *806*(2), 271. https://doi.org/10.1088/0004-637X/806/2/271

Temmer, M. (2021). Space weather: The solar perspective. *Living Reviews in Solar Physics*, *18*(1), 4. https://doi.org/10.1007/s41116-021-00030-3

Török, T., Downs, C., Linker, J. A., Lionello, R., Titov, V. S., Mikić, Z., et al. (2018). Sun-to-Earth MHD simulation of the 2000 July 14 "Bastille day" eruption. *The Astrophysical Journal*, *856*(1), 75. https://doi.org/10.3847/1538-4357/aab36d

Tsurutani, B. T., Gonzalez, W. D., Tang, F., Akasofu, S. I., & Smith, E. J. (1988). Origin of interplanetary southward magnetic fields responsible for major magnetic storms near solar maximum (1978–1979). *Journal of Geophysical Research*, *93*(A8), 8519–8531. https://doi.org/10.1029/JA093iA08p08519

Verbeke, C., Mays, M. L., Temmer, M., Bingham, S., Steenburgh, R., Dumbović, M., et al. (2019). Benchmarking CME arrival time and impact: Progress on metadata, metrics, and events. *Space Weather*, *17*(1), 6–26. https://doi.org/10.1029/2018SW002046

Vršnak, B., Žic, T., Vrbanec, D., Temmer, M., Rollett, T., Möstl, C., et al. (2013). Propagation of interplanetary coronal mass ejections: The drag-based model. *Solar Physics*, *285*(1–2), 295–315. https://doi.org/10.1007/s11207-012-0035-4

Wang, Y., Liu, J., Jiang, Y., & Erdélyi, R. (2019). CME arrival time prediction using convolutional neural network. *The Astrophysical Journal*, *881*(1), 15. https://doi.org/10.3847/1538-4357/ab2b3e

Winslow, R. M., Scolini, C., Lugaz, N., & Galvin, A. B. (2021). The effect of stream interaction regions on ICME structures observed in longitudinal conjunction. *The Astrophysical Journal*, *916*(1), 40. https://doi.org/10.3847/1538-4357/ac0439

Xue, X. H., Wang, Y., Ye, P. Z., Wang, S., & Xiong, M. (2005). Analysis on the interplanetary causes of the great magnetic storms in solar maximum (2000–2001). *Planetary and Space Science*, *53*(4), 443–457. https://doi.org/10.1016/j.pss.2004.10.002

Yurchyshyn, V., Yashiro, S., Abramenko, V., Wang, H., & Gopalswamy, N. (2005). Statistical distributions of speeds of coronal mass ejections. *The Astrophysical Journal*, *619*(1), 599–603. https://doi.org/10.1086/426129